

# Guiding a diffusion model with itself using sliding windows

Nikolas Adaloglou  
adaloglo@hhu.de

Heinrich Heine University  
Düsseldorf, Germany

Tim Kaiser  
tikai103@hhu.de

Damir Iagudin  
damir.iagudin@hhu.de

Markus Kollmann  
markus.kollmann@hhu.de

---

## Abstract

Guidance is a widely used technique for diffusion models to enhance sample quality. Technically, guidance is realised by using an auxiliary model that generalises more broadly than the primary model. Using a 2D toy example, we first show that it is highly beneficial when the auxiliary model exhibits similar but stronger generalisation errors than the primary model. Based on this insight, we introduce *masked sliding window guidance* (M-SWG), a novel, training-free method. M-SWG upweights long-range spatial dependencies by guiding the primary model with itself by selectively restricting its receptive field. M-SWG requires neither access to model weights from previous iterations, additional training, nor class conditioning. M-SWG achieves a superior Inception score (IS) compared to previous state-of-the-art training-free approaches, without introducing sample oversaturation. In conjunction with existing guidance methods, M-SWG reaches state-of-the-art Fréchet DINOv2 distance on ImageNet using EDM2-XXL and DiT-XL. The code is available at [https://github.com/HHU-MMBS/swg\\_bmvc2025\\_official](https://github.com/HHU-MMBS/swg_bmvc2025_official).

## Introduction

Diffusion models (DMs) have emerged as a powerful approach for generative tasks, achieving remarkable success in areas such as image synthesis and text-to-image generation [1, 2, 3, 4, 5, 6]. Despite their success, DMs often fail to generate high-quality samples [7] and require guidance techniques to improve visual fidelity (Fig. 1). The currently most popular method, classifier-free guidance (CFG), pushes the sample towards regions with higher posterior class probability [8]. Unlike its predecessor, classifier guidance [9], which relies on training an external classifier on labeled noisy images, CFG combines conditional and unconditional denoisers, which can be trained jointly [8].

In the following, we denote by  $\mathbf{x}$  a noisy image and by  $\boldsymbol{\epsilon}(\mathbf{x}, t; c)$  and  $\boldsymbol{\epsilon}(\mathbf{x}, t)$  the class conditional and unconditional noise predictors at timestep  $t$  of the denoising process [9]. CFG

combines the two noise predictions during sampling using the linear extrapolation scheme

$$\tilde{\boldsymbol{\epsilon}}(\mathbf{x}, t; c) = \boldsymbol{\epsilon}(\mathbf{x}, t; c) + w[\boldsymbol{\epsilon}(\mathbf{x}, t; c) - \boldsymbol{\epsilon}(\mathbf{x}, t)], \quad \text{with guidance weight } w > 0. \quad (1)$$

Therefore, CFG can be viewed as a linear extrapolation method [10, 46]. Equivalent extrapolation schemes can be found for all diffusion model formulations, such as target prediction or flow matching [22, 43].

**Limitations of CFG.** Despite the widespread use of CFG in conditional synthesis [35], it comes with notable limitations. First, it increases the training budget. When trained jointly, the unconditional task can consume up to 20% of the computational cost [15]. Additionally, while CFG reduces class mismatch between samples and conditions of the noise predictor [42], this benefit comes at the expense of sample diversity, as sampling focuses on regions with high class probability [23]. Since guidance is a linear extrapolation scheme, the sampling trajectory can overshoot the desired distribution, leading to oversaturated or oversimplified images [28]. Finally, CFG sampling is restricted to class-conditional generation by design.

**Weak model guidance.** Recently, a new class of guidance methods has been developed that addresses some of the limitations of CFG. These methods utilize the linear extrapolation scheme of CFG, given by

$$\tilde{\boldsymbol{\epsilon}}(\mathbf{x}, t) = \boldsymbol{\epsilon}_{\text{pos}}(\mathbf{x}, t) + w[\boldsymbol{\epsilon}_{\text{pos}}(\mathbf{x}, t) - \boldsymbol{\epsilon}_{\text{neg}}(\mathbf{x}, t)], \quad (2)$$

in a more generic way. Here, the subscripts *pos* for positive and *neg* for negative refer to the sign of the noise predictors. The idea behind Equation (2) is to extrapolate into high likelihood regions by designing a negative model  $\boldsymbol{\epsilon}_{\text{neg}}$  that has an inferior performance compared to a well-performing DM  $\boldsymbol{\epsilon}_{\text{pos}}$ . Typically,  $\boldsymbol{\epsilon}_{\text{neg}}$  is derived from  $\boldsymbol{\epsilon}_{\text{pos}}$  by re-training using fewer parameters, architecture-based heuristic manipulations, or shorter training times [10, 23]. We refer to this class of guidance methods as *weak model guidance (WMG)*. While WMG methods seem promising, they often require training additional models, or careful manual selection of specific layers to impair [10].

In this paper, we first introduce a toy example to show that (i) WMG samples closer to high likelihood regions than CFG and (ii) guidance works best if  $\boldsymbol{\epsilon}_{\text{neg}}$  makes similar errors as  $\boldsymbol{\epsilon}_{\text{pos}}$  but stronger. A similar effect can be achieved under increased weight regularization in high-resolution image synthesis. Additionally, we introduce masked sliding window guidance (M-SWG), a novel guidance method designed to upweight long-range dependencies (Fig. 1). In contrast to existing guidance techniques [10, 15, 23, 28, 40, 42, 50], M-SWG requires neither training nor class conditioning and can be applied to any DM that can process multiple image resolutions. M-SWG achieves a superior IS score without causing oversaturation, while maintaining competitive Frchet distances. Finally, by



**Figure 1: Method overview.** **Left:** Even state-of-the-art diffusion models can fail to generate globally coherent images without guidance. **Right:** Sliding window guidance (SWG) upweights long-range dependencies and thereby improves global coherence on average.

combining M-SWG with existing guidance techniques [15, 23], a state-of-the-art Frchet DINOv2 distance (FDD) on ImageNet is achieved using EDM2-XXL and DiT-XL [24, 35].

## 2 Related work

Diffusion sampling can be coarsely divided into CFG-based variations and alternative methods. Vanilla CFG can be improved by adding a noise schedule to the condition [40], introducing monotonically increasing guidance weight schedules [50], stepwise intensity thresholding [42], or applying CFG only at an interval in the intermediate denoising steps [28]. Despite recent advancements, CFG cannot be used with unlabelled datasets or conditional-only trained denoisers by design. While several sampling methods focus on modifying CFG [28, 39, 40, 42, 50], training- and condition-free approaches remain an open quest [41].

Alternative guidance methods can be roughly grouped into three categories: i) *architecture-based impairments*, ii) *image-level manipulations* [18], and iii) *inferior capacity models*, which we refer to as *weak models*. Architectural impairments typically leverage self-attention maps [2, 47] that are known to capture structure-related information [2, 6, 13, 60]. For instance, a handful of manually picked attention maps can be replaced with an identity matrix [2] or filtered using Gaussian smoothing [47]. Nonetheless, the choice of attention maps depends on the model architecture, which limits the applicability of the method. Finally, architecture-specific impairments can create significant side effects, such as deteriorating the visual structure [47]. Image-level manipulations such as frequency filtering have been attempted with limited success [18]. Hong et al. [18] restrict high-frequency filtering to image patches corresponding to high activation areas, achieved by upsampling self-attention maps. However, similar to architecture-based impairments, it requires cherry-picking while being prone to artifacts [47].

Weak models of inferior capacity compared to the positive model can be constructed by limiting the network size (i.e. number of parameters) or its training time [23]. However, such approaches require additional training from scratch or various weight instances, which are not always available. Concurrent work [9] deteriorates the positive model by fine-tuning with its own generated samples to derive the negative model. Different from prior works [9, 23], we aim to systematically study WMG methods, starting with a toy example. Our analysis reveals that the negative model needs to exhibit *a similar modeling error as the positive model, but stronger*. The latter statement has not been explicitly formulated in prior works [9, 18, 23].

## 3 CFG and WMG are fundamentally different

In the following, we introduce a two-dimensional toy example (Fig. 2) to visualize the conceptual differences between CFG and WMG. The data distribution of our toy example consists of three data points  $\mathcal{D} = \{\mathbf{y}_1, \mathbf{y}_2, \mathbf{y}_3\}$ , where each data point is assigned a different class label  $c \in \{1, 2, 3\}$ . We can generate trajectories  $\mathbf{x}(t)$  by numerically solving the ordinary differential equation (ODE)  $d\mathbf{x}(t) = \boldsymbol{\varepsilon}^*(\mathbf{x}(t), \sigma(t))d\sigma(t)$ , with  $\boldsymbol{\varepsilon}^*$  the optimal noise predictor in the Bayesian sense, and  $\sigma(t) \in [0, \sigma_{max}]$  the current noise level.

Note that  $d\sigma(t) < 0$  along a denoising trajectory. It can be shown that for a finite set of  $N$  data points, the optimal noise predictor takes the explicit form [27]

$$\boldsymbol{\varepsilon}^*(\mathbf{x}, \sigma(t)) = \frac{1}{\sigma(t)} \sum_{i=1}^N (\mathbf{x} - \mathbf{y}_i) p(\mathbf{y}_i | \mathbf{x}, t), \quad p(\mathbf{y}_i | \mathbf{x}, t) = \frac{\mathcal{N}(\mathbf{x} | \mathbf{y}_i, \sigma(t)^2)}{\sum_{i=1}^N \mathcal{N}(\mathbf{x} | \mathbf{y}_i, \sigma(t)^2)}, \quad (3)$$

where  $\mathcal{N}(\cdot | \cdot)$  denotes an isotropic normal distribution. That is, the optimal noise predictor is the normalised residual between  $\mathbf{x}$  and the posterior-mean  $\sum_{i=1}^N \mathbf{y}_i p(\mathbf{y}_i | \mathbf{x}, t)$  as an estimator

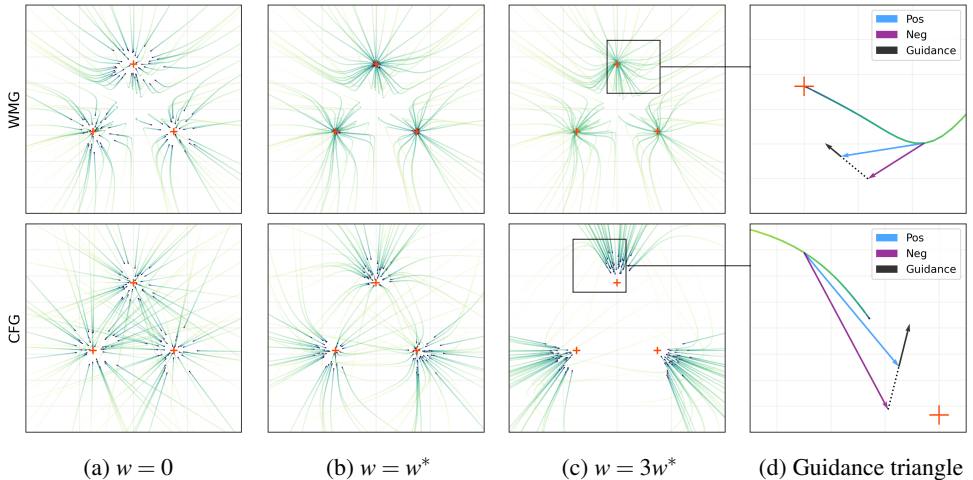


**Figure 2: Inference trajectories for our 2D-toy model. From left to right: (a)**  $w = 0$  yields the trajectories of the positive model. **(b)**  $w^*$  denotes the guidance weight that leads to best (CFG) or onset of saturating (WMG) performance ( $w^* = 1$  for CFG and  $w^* = 5$  for WMG). **(c)** For large guidance weights, CFG exhibits large endpoint errors, while WMG keeps small endpoint errors until it becomes unstable. **(d)** Enlarged views for single trajectories. Arrows show target prediction for a point on the trajectory. In this instance, the guidance correction (black arrow) pushes WMG closer to the data point, unlike CFG.

for a data point. The optimal noise predictor generates trajectories with endpoints arbitrarily close to one of the data points if the ODE is initialized with  $\mathbf{x}_{init} \sim \mathcal{N}(\mathbf{x}|\mathbf{0}, \sigma_{max}^2)$  and  $\sigma_{max}$  is sufficiently large.

Assume we are given an error-prone noise predictor,  $\boldsymbol{\varepsilon}_{err}$ , whose endpoints are distributed as a superposition of three normal distributions, all with variance  $\delta^2$ , and each normal distribution centered around a different data point (Fig. 2a). For this special case it can be shown that  $\boldsymbol{\varepsilon}_{err}(\mathbf{x}, \sigma(t)) = \sigma(t)/\tilde{\sigma}(t)\boldsymbol{\varepsilon}(\mathbf{x}, \tilde{\sigma}(t))$ , with  $\tilde{\sigma}(t)^2 = \sigma(t)^2 + \delta^2$ . The question is now, to what extent CFG and WMG can help to shift the trajectory endpoints of the error-prone predictor closer to the data distribution? To answer this question, we introduce the error-prone predictors  $\boldsymbol{\varepsilon}_{pos}$ ,  $\boldsymbol{\varepsilon}_{neg}$ , and adjust the guidance weight  $w$  of Equation (2) such that the average endpoint error is minimized. Using  $\boldsymbol{\varepsilon}(\mathbf{x}, t) := \boldsymbol{\varepsilon}(\mathbf{x}(t), \sigma(t))$  for brevity, we recover the CFG setting by introducing the class-conditional noise predictor  $\boldsymbol{\varepsilon}_{pos}(\mathbf{x}, t) = \boldsymbol{\varepsilon}_{err}(\mathbf{x}, t; c)$  and the unconditional noise predictor  $\boldsymbol{\varepsilon}_{neg}(\mathbf{x}, t) = \boldsymbol{\varepsilon}_{err}(\mathbf{x}, t)$ . Likewise we recover the WMG setting by  $\boldsymbol{\varepsilon}_{pos}(\mathbf{x}, t) = \boldsymbol{\varepsilon}_{err}(\mathbf{x}, t)$  and  $\boldsymbol{\varepsilon}_{neg}(\mathbf{x}, t) = \boldsymbol{\varepsilon}'_{err}(\mathbf{x}, t)$ , where  $\boldsymbol{\varepsilon}'_{err}$  differs from  $\boldsymbol{\varepsilon}_{err}$  by a larger endpoint variance  $\delta' > \delta$ . The denoising trajectories shown in Fig. 2 follow from numerically solving the ODE for  $\mathbf{x}(t)$ , using Equation (2) instead of the optimal noise predictor.

**CFG.** As we use just one datapoint per class, the class conditional noise predictor is given by  $\boldsymbol{\varepsilon}_{pos}(\mathbf{x}, t) = \sigma(t)^{-1}(\mathbf{x} - \mathbf{y}_{i_c})$ , with  $i_c$  the data point index belonging to class  $c$ , resulting in the special case of straight lines as denoising trajectories (Fig. 2a, CFG). For small guidance weights, the trajectory endpoints match slightly better to the data distribution (Fig. 2b, CFG), but for larger guidance weights, they move away from the data distribution (Fig. 2c, CFG). This behavior is a consequence of the fact that  $\boldsymbol{\varepsilon}_{pos}$  drives the trajectory towards the data point with the corresponding class label, whereas  $\boldsymbol{\varepsilon}_{neg}$  denoises in the direction of a weighted superposition of all data points. As a result, CFG tends to shift the trajectories away from

the center of mass of the data distribution (Fig. 2d, CFG), favoring classifiable endpoints over a fit to the data distribution. This behavior has been described in previous works [15] and scales to higher dimensions, e.g. images, where a better distribution overlap between generated samples and training samples in feature space is only observed for sufficiently small guidance weights.

**WMG.** In contrast to CFG, increasing the guidance weight for WMG drives trajectory endpoints closer to the data distribution (Fig. 2a-c, WMG), up to the point where trajectories become unstable. The crucial condition for WMG to work well is that, in each step, the prediction of  $\boldsymbol{\epsilon}_{\text{pos}}$  is closer to  $\boldsymbol{\epsilon}^*$  than the prediction of  $\boldsymbol{\epsilon}_{\text{neg}}$ , causing the extrapolation to correct the prediction of  $\boldsymbol{\epsilon}_{\text{pos}}$  towards the optimal prediction of  $\boldsymbol{\epsilon}^*$  (Fig. 2d, WMG).

$$w^*(\mathbf{x}, t) = \frac{\|\boldsymbol{\epsilon}_{\text{pos}}(\mathbf{x}, t) - \boldsymbol{\epsilon}^*(\mathbf{x}, t)\|}{\|\boldsymbol{\epsilon}_{\text{pos}}(\mathbf{x}, t) - \boldsymbol{\epsilon}_{\text{neg}}(\mathbf{x}, t)\|} \quad (4)$$

For the special case that  $\boldsymbol{\epsilon}_{\text{pos}}$  and  $\boldsymbol{\epsilon}_{\text{neg}}$  exhibit the same error up to a multiplicative factor, it is possible for WMG to closely recover the prediction of the optimal denoiser  $\boldsymbol{\epsilon}^*$ , under the optimal guidance weight  $w^*(\mathbf{x}, t)$  (Equation (4) and supplementary material). The optimal weight is obviously of little practical use as it requires knowledge about the optimal noise predictor  $\boldsymbol{\epsilon}^*$ . However, it illustrates that the practical choice of a constant guidance weight is, in general, an *ad hoc* simplification. Surprisingly, we observe excellent, albeit imperfect, matching between endpoints and datapoints for constant but sufficiently large weights (Fig. 2).

## 4 Sliding window guidance (SWG)

Assuming that a significant source of the predictor’s error can be attributed to long-range dependencies, we introduce a new guidance method that aims to correct such errors. The idea is to generate  $\boldsymbol{\epsilon}_{\text{neg}}$  by restricting the spatial input size ( $H \times W$ ) of  $\boldsymbol{\epsilon}_{\text{pos}}$  to a smaller size  $k \times l$ , with  $k < H$  and  $l < W$ , which induces a defined cut-off for long-range dependencies. We use sliding windows to generate  $N$  crops of size  $k \times l$ , using a fixed stride  $s$  per dimension. These crops are independently processed (without rescaling) by  $\boldsymbol{\epsilon}_{\text{pos}}$  as illustrated in Fig. 3. The  $N$  predictions of  $\boldsymbol{\epsilon}_{\text{pos}}$  are superimposed in the same order and at the same positions, which results in an  $H \times W$  output for  $\boldsymbol{\epsilon}_{\text{neg}}$ . Overlapping pixels are averaged. A pseudo-code for

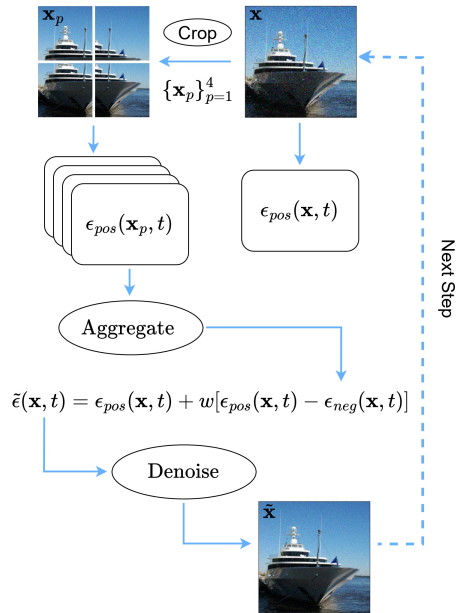


Figure 3: **An illustration of sliding window guidance (SWG).** We use  $\boldsymbol{\epsilon}_{\text{pos}}$  to independently process  $N = 4$  overlapping image crops.  $\boldsymbol{\epsilon}_{\text{neg}}$  is generated by superimposing the processed crops and averaging the overlapping pixels.

A pseudo-code for

SWG is provided in the supplementary material. We emphasize that using sliding windows is a common technique in high-resolution 2D/3D image processing [6, 8, 20, 58, 44].

**Hyperparameters and limitations.** One limitation of SWG is that  $\epsilon_{\text{pos}}$  must process inputs of varying image resolution. Nonetheless, current architectures, such as Unets [14] or (diffusion) image transformers [5], generally satisfy this requirement. SWG can be implemented in a few lines of code and requires no training-related modifications or class conditioning. Unless otherwise specified, we assume  $H = W$  and use crop size  $k = l \approx 5/8 \times H$  and  $N = 4$ , which translates into  $k = 40, s = 24$  at  $64 \times 64$  resolution. We denote the overlap ratio per dimension as  $r = 1 - \frac{s}{k} = 0.4$ .

**SWG in latent DMs.** We keep the same design choices for latent DMs [57] that operate in  $\frac{H}{8} \times \frac{H}{8}$  feature dimensions, where 8 is the upscaling/downscaling factor. More specifically, SWG is performed in each denoising step in the low-dimensional latent space (i.e.  $64 \times 64$ ), and the final output is passed to the decoder. The decoder handles the upscaling to the image dimensions, i.e., from  $64 \times 64$  to  $512 \times 512$ . The rationale behind SWG operating in lower feature dimensions is that latent representations, i.e., of a VAE, preserve to a significant extent the spatial structure of the image [12, 26]. To make SWG compatible with DiT, we add positional encoding interpolation to process the crops. The choice of  $k \approx \frac{5}{8}H$  is determined by practical considerations of Unets. Specifically,  $k$  must satisfy  $\frac{k}{2^n} \in \mathbb{N}$ , where  $n$  is the number of downsampling steps of the Unet, and the diffusion model  $\epsilon_{\text{pos}}$  must be able to process multiple image resolutions.

**Computational overhead.** The computational overhead of SWG compared to CFG is determined by the overlap ratio  $r$  and the architecture. For EDM-S and  $r = 0.4$ , we measured an overhead of less than 30% compared to CFG based on a naive implementation of SWG. More details are provided in the supplementary material.

**Masked SWG (M-SWG).** We experimentally observe that applying guidance only to overlapping regions of the sliding windows shows better performance than applying guidance to the whole image. We therefore introduce a binary mask  $\mathbf{M} \in \{0, 1\}^{H \times W}$  to filter for overlapping regions when applying guidance,  $\tilde{\epsilon}(\mathbf{x}, t) = \epsilon_{\text{pos}}(\mathbf{x}, t) + w\mathbf{M} \odot [\epsilon_{\text{pos}}(\mathbf{x}, t) - \epsilon_{\text{neg}}(\mathbf{x}, t)]$ .

**Combining SWG with existing methods.** Since SWG and M-SWG are conceptually different from existing techniques, we investigate whether they can enhance existing techniques as a linear combination of their stepwise outcomes [29]. Mathematically,

$$\tilde{\epsilon}(\mathbf{x}, t) = \epsilon_{\text{pos}}(\mathbf{x}, t) + \sum_i w_i [\epsilon_{\text{pos}}(\mathbf{x}, t) - \epsilon_{\text{neg}}^{(i)}(\mathbf{x}, t)], \quad (5)$$

where  $i$  indicates different guidance methods. Quantitative improvements would suggest a complementary relationship between methods. For instance, combining CFG with SWG would increase noise-condition alignment whilst conforming to long-range dependencies.

## 5 Experimental evaluation and discussion

**Diffusion guidance baselines.** We divide the evaluation into training-free methods (Table 1) and state-of-the-art comparisons (Table 2), where M-SWG is used in conjunction with existing methods (Equation (5)). Regarding training-free methods, we consider reduced training (RT) as a state-of-the-art baseline [23], along with sampling without guidance ( $w = 0$ ). Nonetheless, publicly available DMs do *not* always offer earlier weight instances such as DiT-XL [65] and StableDiffusion [67], and thus RT cannot be applied. When combining

Model	Guidance	FID	FDD
EDM2 S-512	$\times$	2.91	112
	RT <sub>.8/1.2</sub>	<b>1.79</b>	46.5
	SWG <sub>.1/5</sub>	2.59	56.1
	M-SWG <sub>.2/1.1</sub>	2.55	53.4
	RT <sub>.8/1.2</sub> + M-SWG <sub>0/.25</sub>	1.79	<b>40.9</b>
EDM2 XXL-512	$\times$	2.29	49.7
	RT <sub>.1/1.3</sub>	<b>2.26</b>	34.6
	SWG <sub>.05/.2</sub>	2.61	37.7
	M-SWG <sub>.05/.5</sub>	2.46	36.8
	RT <sub>.1/1.05</sub> + M-SWG <sub>0/.1</sub>	2.26	<b>32.9</b>
DiT XL-256	$\times$	9.83	213
	SWG <sub>.25/.5</sub>	4.00	80.6
	M-SWG <sub>.5/1.5</sub>	<b>3.30</b>	<b>70.3</b>
<i>Unconditional generation</i>			
EDM2 S-512	$\times$	13.7	250
	RT <sub>.1.6/2</sub>	<b>4.89</b>	107.8
	SWG <sub>.3/.5</sub>	10.2	167.4
	M-SWG <sub>.5/.9</sub>	9.32	149.4
	RT <sub>.1.6/1.35</sub> + M-SWG <sub>0/.15</sub>	4.89	<b>101.2</b>

Table 1: Training-free diffusion guidance sampling methods comparison.

**Tables 1-2: We report FDD ( $\downarrow$ ) and FID ( $\downarrow$ ) on ImageNet for several benchmarks.** The subscripts indicate the chosen guidance scale that yields the optimal guidance weights for FID/FDD based on a hyperparameter search.

Model	Guidance	FDD
EDM2 S-512	RCT <sub>1.4</sub>	42.1
	RCT <sub>1</sub> + SWG <sub>.2</sub>	39.2
	RCT <sub>1.2</sub> + M-SWG <sub>.14</sub>	<b>39.1</b>
	CFG <sub>.8</sub> <sup>†</sup>	52.9
	CFG <sub>.3</sub> <sup>†</sup> + M-SWG <sub>.3</sub>	<b>51.9</b>
EDM2 XXL-512	RCT <sub>1</sub>	30.3
	RCT <sub>.9</sub> + M-SWG <sub>.05</sub>	<b>29.8</b>
	CFG <sub>.4</sub> <sup>†</sup>	36.7
	CFG <sub>.2</sub> <sup>†</sup> + M-SWG <sub>.05</sub>	<b>36.2</b>
DiT XL-256	CFG <sub>2.05</sub>	54.3
	CFG <sub>.7</sub> + SWG <sub>.1</sub>	50.6
	CFG <sub>.6</sub> + M-SWG <sub>.5</sub>	<b>49.1</b>
<i>Unconditional generation</i>		
EDM2 S-512	RCT <sub>1.8</sub>	97.9
	RCT <sub>1.3</sub> + M-SWG <sub>.15</sub>	<b>91.8</b>

Table 2: M-SWG enhances existing state-of-the-art methods. The dagger † indicates that a smaller capacity model is used.

M-SWG with other non-training-free state-of-the-art methods (Equation (5)), we adopt CFG and the recent approach of reducing training time and learning capacity (*RCT*), also known as “*autoguidance*” [23]. We emphasize that CFG requires jointly or independently training a conditional and an unconditional denoiser, and it is thus not training-free.

**Implementation details.** The experiments were conducted on 4 Nvidia A100 GPUs with 40GB of VRAM. Following recent works [9, 19, 23, 24, 28, 47], we produce 50K samples for the evaluations and measure the Frechet distance [24] using features from InceptionV3 and DINOv2 ViT-L [52], denoted by FID and FDD, respectively. We use FDD as our primary metric since it has shown better alignment with human judgment [27, 30, 34, 47]. We also report the inception score (IS) as a measure of visual quality. We apply SWG and M-SWG to state-of-the-art models, such as DiT-XL [35], and EDMv2 [24].

Regarding EDM2, we set the EMA-like hyperparameter to 0.1 to make our analysis more generally applicable. Following Karras et al. [23], we use  $T/16$  for EDM2-S and  $T/3.5$  for EDM2-XXL for the negative model when applying RT and RCT, where  $T$  is the training time of the positive model. When applying CFG to EDM2 models, we use a smaller capacity unconditional model (EDM2-XS), which we denote as CFG<sup>†</sup>. Additional implementation details are provided in the supplementary material.

**M-SWG versus training-free methods.** In Table 1, we observe significant gains compared to the unguided generation using SWG and M-SWG. M-SWG provides a competitive alternative when previous weight instances, such as with DiT-XL, are unavailable. We believe that the inferior Frechet distances from SWG/M-SWG are attributed to background

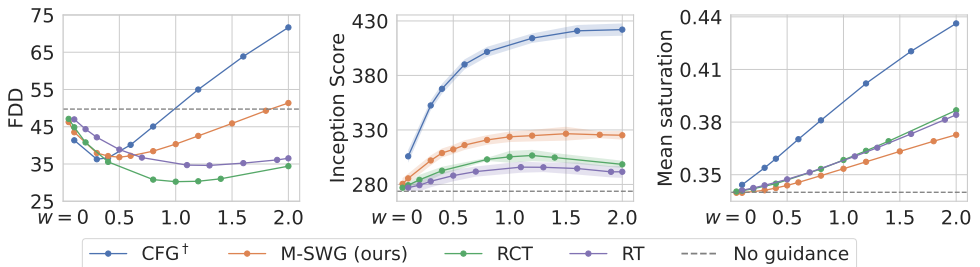


Figure 4: **Visualizing the achieved tradeoff by varying the guidance scale  $w$  (x-axis) for FDD ( $\downarrow$ , left), Inception score (IS  $\uparrow$ , center), and saturation ( $\downarrow$ , right) using EDM2-XXL. M-SWG achieves superior perceptual quality as measured by the IS compared to RT and RCT, while not exhibiting undesired oversaturation as CFG $^\dagger$ , on average.**

N, k, r	FDD	FID
$\mathbf{x}$	112.2	2.92
4, 32, 0	55.7 <sub>0.3</sub>	2.72 <sub>0.1</sub>
4, 40, 0.4	56.1 <sub>0.5</sub>	2.59 <sub>0.1</sub>
4, 48, 0.6	60.7 <sub>0.5</sub>	<b>2.56</b> <sub>0.1</sub>
9, 32, 0.5	<b>55.4</b> <sub>0.3</sub>	2.69 <sub>0.1</sub>
9, 24, 0.63	58.1 <sub>0.2</sub>	2.89 <sub>0.1</sub>
16, 16, 0	64.0 <sub>0.2</sub>	3.15 <sub>0.1</sub>

Table 3: Varying kernel size  $k$  and number of crops  $N$ .

Guidance	Interval	FDD
$\mathbf{x}$	-	112.2
RT <sub>1.2</sub>	-	46.5
+ interval <sub>1.8</sub>	10-20	<b>43.8</b>
SWG <sub>0.5</sub>	-	56.1
+ interval <sub>1.2</sub>	15-20	51.3
M-SWG <sub>1.1</sub>	-	53.4
+ interval <sub>1.7</sub>	13-23	51.7

Table 4: Applying guidance only at an interval (32 steps).

	FDD	FID
CFG $^\dagger$ [10]	52.9 <sub>0.8</sub>	2.44 <sub>0.1</sub>
<i>WMG methods</i>		
a) Reduced training	46.5 <sub>1.2</sub>	1.79 <sub>0.8</sub>
b) Reduced capacity	70.0 <sub>1.4</sub>	2.20 <sub>0.7</sub>
c) RCT (a + b)	<b>42.1</b> <sub>1.4</sub>	<b>1.67</b> <sub>0.8</sub>
d) WD fine-tuning	52.1 <sub>0.6</sub>	2.46 <sub>0.1</sub>
e) WD + (a)	43.9 <sub>0.9</sub>	2.25 <sub>0.2</sub>

Table 5: A comparison of WMG strategies, including the novel weight decay (WD) variants.

**Tables 3-5: Additional experiments on ImageNet-512 using EDM2-S.** The subscripts indicate the chosen guidance scales based on a hyperparameter search.

simplification, which strongly affects the statistics of the image distribution. This is a shared limitation with CFG [10, 15] and can be further investigated in future work. Crucially, by combining RT with M-SWG, we achieve a new state-of-the-art FDD for training-free image synthesis using EDM2-XXL (32.9), which also outperforms CFG (36.7). The gains in FDD do not translate to FID. We hypothesize that the less-trained negative model (RT) makes more errors related to local image details, complementing SWG, and it is best captured in the DINOv2 feature space. Finally, no training-free approach can significantly outperform the unguided EDM2-XXL FID score. This is linked to existing concerns that FID does not reflect gradual improvements [11, 19, 27, 34, 41], as well as that the EDM2-XXL makes fewer errors that can be corrected with guidance techniques.

Similar to EDM2, applying M-SWG to DiT is highly beneficial in terms of FID/FDD. To the best of our knowledge, early training weight instances are not publicly available for DiT to benchmark against RT or other WMG variants. The poor performance of the unguided DiT-XL is mainly attributed to the joint training on both conditional and unconditional generation, which may reduce network capabilities and lead to skewed sampling distributions [23].

**State-of-the-art comparison.** Table 2 shows consistent improvements when combining M-SWG with other state-of-the-art methods. A large relative FDD gain of 9.6% is found when combining M-SWG with CFG using DiT-XL. Compared to using M-SWG in conjunction with RT versus RCT, the relative gain decreases from 4.9% to 1.6%. This suggests

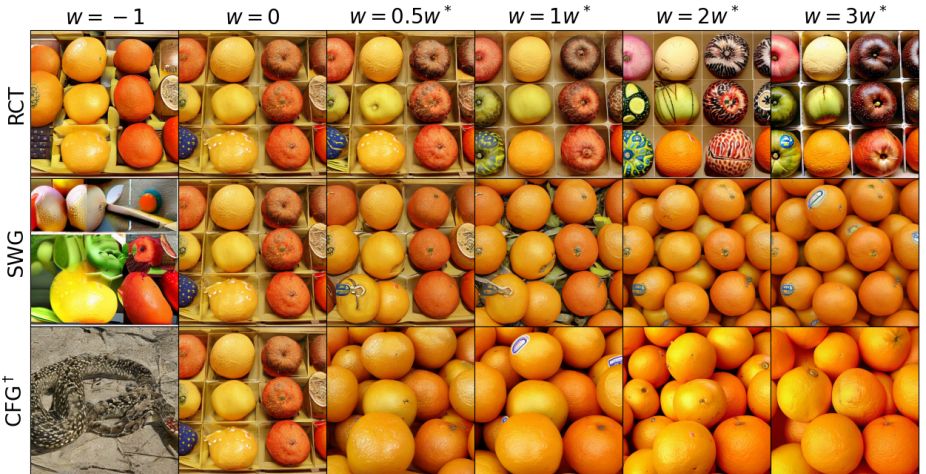


Figure 5: **Samples generated by different guidance methods (rows) with different guidance weights (columns) but the same initial noise and condition (orange class) using EDM2-XXL.** Guidance weights  $w$  are scaled by  $w^*$ , the individual weight for each method corresponding to the lowest FDD. The first column shows samples using  $\epsilon_{neg}$ , which corresponds to setting  $w = -1$  in Eq. (2).

that the model of reduced learning capacity partially accounts for the correction in long-range dependencies. Finally, M-SWG shows significant improvements on the unconditional benchmarks. Future work can explore SWG and M-SWG for text-conditioned DMs.

**Quality-diversity tradeoffs.** To investigate the achieved tradeoff of M-SWG, we plot  $w$  against FDD, IS score, and saturation in Fig. 4. Saturation is quantified as the mean channel intensity in HSV color space (S channel), as in [49]. While RT and RCT are slightly superior in terms of FDD, M-SWG achieves a better image quality (IS) across guidance scales. Intriguingly, we find that M-SWG does not suffer from oversaturation, unlike the CFG and RCT. A low saturation is preferred because it is closer to the statistics of real images (0.32 on the ImageNet test set). Moreover, the root mean square contrast of the samples (the standard deviation of intensities after greyscale conversion [36, 39]) demonstrates an even more pronounced disparity between M-SWG and other methods (see supplementary material). Overall, the smaller FID improvements of M-SWG (e.g. 2.55 versus 2.91 for EDM2-S in Table 1), while achieving a higher IS score than RC, RCT suggests that the merits of M-SWG are more in improving semantic coherence than diversity of images.

**Additional experiments.** Table 3 shows that several combinations of kernel size and  $N$  crops can attain similar results on both FID and FDD. Intriguingly, while FID prefers higher overlap ratios  $r$  (for  $N = 4$ ), FDD shows that the overlap between crops is not required to obtain improvements over the unguided model. This suggests that (i) even without overlapping crops, SWG introduces no severe artifacts w.r.t. generative metrics, and (ii) minimal to no tuning is required as opposed to heuristic model-specific impairments like SAG or PAG [2, 18]. Moreover, in Table 4, we demonstrate that applying guidance only at an intermediate interval further enhances SWG and M-SWG.

**Same error but stronger in high dimensions.** Motivated by the toy model, we verify its implication in higher dimensions by constructing  $\epsilon_{neg}$  with the same network architecture as  $\epsilon_{pos}$ , but with significantly increased weight regularization. This can be implemented

by either fine-tuning  $\epsilon_{\text{pos}}$ , denoted as *Weight decay (WD) fine-tuning*, or by re-training it with very little compute time, which we call *WD with reduced training*. WD increases the model’s bias in the context of the bias-variance tradeoff [49]. Naive training-free approaches such as dropout or quantization to construct  $\epsilon_{\text{neg}}$  have been unsuccessful [23]. Experimental results are presented in Table 5. Interestingly, WD with reduced training performs comparably with the current state-of-the-art RCT, demonstrating that it is another principled way of constructing  $\epsilon_{\text{neg}}$ .

**Qualitative results.** To visualize the differences between the guidance methods, we examine ImageNet-512 samples generated from the same initial noise in Fig. 5. All three methods, RCT, SWG, and CFG<sup>†</sup>, tend to exhibit improved perceptual quality for moderate guidance weights but show reduced variation (SWG, CFG<sup>†</sup>) or artifacts (RCT) for higher guidance weights. To understand these effects, it is helpful to examine the unguided samples produced by  $\epsilon_{\text{neg}}$ , which corresponds to setting  $w = -1$  in Equation (2). For example, comparing the first two columns of Fig. 5, we see that the image composition (e.g. box of fruits) for  $\epsilon_{\text{pos}}$  ( $w = 0$ ) is only maintained by  $\epsilon_{\text{neg}}$  ( $w = -1$ ) for RCT. Consequently, with increasing  $w$ , RCT meaningfully conserves the image composition, SWG does so slightly, and CFG<sup>†</sup> not at all.

## 6 Conclusion

In this work, we identified the general concept of “same error but stronger” for designing diffusion guidance methods. We validated this concept using a toy example and experimentally in high dimensions using a negative model with increased weight regularization. Additionally, we presented a novel training-free and condition-free guidance method (M-SWG) that enhances global coherence and consistency of objects. M-SWG can be used as a standalone method or combined with state-of-the-art sampling methods, such as CFG, to yield visually appealing and state-of-the-art results in image synthesis.

## Acknowledgements

Computing resources were provided by the German AI Service Center WestAI under the project name “westai9566”. In particular, the authors would like to express their gratitude to Prof. Dr. Timo Dickscheid and Fritz Niesel for their guidance regarding the computational resources used for the project. The authors also wish to thank Kaspar Senft, Georgios Zoumpourlis, and Felix Michels for their constructive feedback, which greatly enhanced the quality of this manuscript.

## References

- [1] Nikolas Adaloglou, Tim Kaiser, Felix Michels, and Markus Kollmann. Rethinking cluster-conditioned diffusion models for label-free image synthesis. In *2025 IEEE/CVF Winter Conference on Applications of Computer Vision (WACV)*, pages 3603–3613. IEEE, 2025.
- [2] Donghoon Ahn, Hyoungwon Cho, Jaewon Min, Wooseok Jang, Jungwoo Kim, Seon-Hwa Kim, Hyun Hee Park, Kyong Hwan Jin, and Seungryong Kim. Self-rectifying dif-

- fusion sampling with perturbed-attention guidance. *arXiv preprint arXiv:2403.17377*, 2024.
- [3] Md Manjurul Ahsan, Shivakumar Raman, Yingtao Liu, and Zahed Siddique. A comprehensive survey on diffusion models and their applications. 2024.
- [4] Sina Alemohammad, Ahmed Imtiaz Humayun, Shruti Agarwal, John Collomosse, and Richard Baraniuk. Self-improving diffusion models with synthetic data. *arXiv preprint arXiv:2408.16333*, 2024.
- [5] Yogesh Balaji, Seungjun Nah, Xun Huang, Arash Vahdat, Jiaming Song, Qinsheng Zhang, Karsten Kreis, Miika Aittala, Timo Aila, Samuli Laine, et al. ediff-i: Text-to-image diffusion models with an ensemble of expert denoisers. *arXiv preprint arXiv:2211.01324*, 2022.
- [6] Omer Bar-Tal, Lior Yariv, Yaron Lipman, and Tali Dekel. Multidiffusion: Fusing diffusion paths for controlled image generation. 2023.
- [7] Arwen Bradley and Preetum Nakkiran. Classifier-free guidance is a predictor-corrector. *arXiv preprint arXiv:2408.09000*, 2024.
- [8] M Jorge Cardoso, Wenqi Li, Richard Brown, Nic Ma, Eric Kerfoot, Yiheng Wang, Benjamin Murrey, Andriy Myronenko, Can Zhao, Dong Yang, et al. Monai: An open-source framework for deep learning in healthcare. *arXiv preprint arXiv:2211.02701*, 2022.
- [9] Min Jin Chong and David Forsyth. Effectively unbiased fid and inception score and where to find them, 2020. URL <https://arxiv.org/abs/1911.07023>.
- [10] Hyungjin Chung, Jeongsol Kim, Geon Yeong Park, Hyelin Nam, and Jong Chul Ye. Cfg++: Manifold-constrained classifier free guidance for diffusion models. *arXiv preprint arXiv:2406.08070*, 2024.
- [11] Prafulla Dhariwal and Alexander Nichol. Diffusion models beat gans on image synthesis. *Advances in neural information processing systems*, 34:8780–8794, 2021.
- [12] Sander Dieleman. Generative modelling in latent space, 2025. URL <https://sander.ai/2025/04/15/latents.html>.
- [13] Amir Hertz, Ron Mokady, Jay Tenenbaum, Kfir Aberman, Yael Pritch, and Daniel Cohen-Or. Prompt-to-prompt image editing with cross attention control. *arXiv preprint arXiv:2208.01626*, 2022.
- [14] Martin Heusel, Hubert Ramsauer, Thomas Unterthiner, Bernhard Nessler, and Sepp Hochreiter. Gans trained by a two time-scale update rule converge to a local nash equilibrium, 2018.
- [15] Jonathan Ho and Tim Salimans. Classifier-free diffusion guidance, 2022. URL <https://arxiv.org/abs/2207.12598>.
- [16] Jonathan Ho, Ajay Jain, and Pieter Abbeel. Denoising diffusion probabilistic models, 2020.

- [17] Susung Hong. Smoothed energy guidance: Guiding diffusion models with reduced energy curvature of attention. *arXiv preprint arXiv:2408.00760*, 2024.
- [18] Susung Hong, Gyuseong Lee, Wooseok Jang, and Seungryong Kim. Improving sample quality of diffusion models using self-attention guidance. In *Proceedings of the IEEE/CVF International Conference on Computer Vision*, pages 7462–7471, 2023.
- [19] Sadeep Jayasumana, Srikumar Ramalingam, Andreas Veit, Daniel Glasner, Ayan Chakrabarti, and Sanjiv Kumar. Rethinking fid: Towards a better evaluation metric for image generation. In *Proceedings of the IEEE/CVF Conference on Computer Vision and Pattern Recognition*, pages 9307–9315, 2024.
- [20] AQ Jiang, A Sablayrolles, A Mensch, C Bamford, DS Chaplot, D de las Casas, F Bressand, G Lengyel, G Lample, L Saulnier, et al. Mistral 7b (2023). *arXiv preprint arXiv:2310.06825*, 2023.
- [21] Jared Kaplan, Sam McCandlish, Tom Henighan, Tom B Brown, Benjamin Chess, Rewon Child, Scott Gray, Alec Radford, Jeffrey Wu, and Dario Amodei. Scaling laws for neural language models. *arXiv preprint arXiv:2001.08361*, 2020.
- [22] Tero Karras, Miika Aittala, Timo Aila, and Samuli Laine. Elucidating the design space of diffusion-based generative models, 2022.
- [23] Tero Karras, Miika Aittala, Tuomas Kynkäänniemi, Jaakko Lehtinen, Timo Aila, and Samuli Laine. Guiding a diffusion model with a bad version of itself, 2024. URL <https://arxiv.org/abs/2406.02507>.
- [24] Tero Karras, Miika Aittala, Jaakko Lehtinen, Janne Hellsten, Timo Aila, and Samuli Laine. Analyzing and improving the training dynamics of diffusion models, 2024. URL <https://arxiv.org/abs/2312.02696>.
- [25] Diederik P. Kingma, Tim Salimans, Ben Poole, and Jonathan Ho. Variational diffusion models, 2023.
- [26] Theodoros Kouzelis, Ioannis Kakogeorgiou, Spyros Gidaris, and Nikos Komodakis. Eq-vae: Equivariance regularized latent space for improved generative image modeling. *arXiv preprint arXiv:2502.09509*, 2025.
- [27] Tuomas Kynkäänniemi, Tero Karras, Miika Aittala, Timo Aila, and Jaakko Lehtinen. The role of imagenet classes in fréchet inception distance, 2023.
- [28] Tuomas Kynkäänniemi, Miika Aittala, Tero Karras, Samuli Laine, Timo Aila, and Jaakko Lehtinen. Applying guidance in a limited interval improves sample and distribution quality in diffusion models, 2024. URL <https://arxiv.org/abs/2404.07724>.
- [29] Nan Liu, Shuang Li, Yilun Du, Antonio Torralba, and Joshua B Tenenbaum. Compositional visual generation with composable diffusion models. In *European Conference on Computer Vision*, pages 423–439. Springer, 2022.
- [30] Stanislav Morozov, Andrey Voynov, and Artem Babenko. On self-supervised image representations for gan evaluation. In *International Conference on Learning Representations*, 2021.

- [31] Jisu Nam, Heesu Kim, DongJae Lee, Siyoon Jin, Seungryong Kim, and Seung-gyu Chang. Dreammatcher: Appearance matching self-attention for semantically-consistent text-to-image personalization. In *Proceedings of the IEEE/CVF Conference on Computer Vision and Pattern Recognition*, pages 8100–8110, 2024.
- [32] Maxime Oquab, Timothée Darcet, Theo Moutakanni, Huy V. Vo, Marc Szafraniec, Vasil Khalidov, Pierre Fernandez, Daniel Haziza, Francisco Massa, Alaaeldin El-Nouby, Russell Howes, Po-Yao Huang, Hu Xu, Vasu Sharma, Shang-Wen Li, Wojciech Galuba, Mike Rabbat, Mido Assran, Nicolas Ballas, Gabriel Synnaeve, Ishan Misra, Herve Jegou, Julien Mairal, Patrick Labatut, Armand Joulin, and Piotr Bojanowski. Dinov2: Learning robust visual features without supervision, 2023.
- [33] D. B. Owen. A table of normal integrals. *Communications in Statistics - Simulation and Computation*, 9(4):389–419, 1980. doi: 10.1080/03610918008812164. URL <https://doi.org/10.1080/03610918008812164>.
- [34] Gaurav Parmar, Richard Zhang, and Jun-Yan Zhu. On aliased resizing and surprising subtleties in gan evaluation, 2022. URL <https://arxiv.org/abs/2104.11222>.
- [35] William Peebles and Saining Xie. Scalable diffusion models with transformers. In *Proceedings of the IEEE/CVF International Conference on Computer Vision*, pages 4195–4205, 2023.
- [36] Eli Peli. Contrast in complex images. *Journal of the Optical Society of America A*, 7(10):2032–2040, 1990.
- [37] Robin Rombach, Andreas Blattmann, Dominik Lorenz, Patrick Esser, and Björn Ommer. High-resolution image synthesis with latent diffusion models. In *Proceedings of the IEEE/CVF conference on computer vision and pattern recognition*, pages 10684–10695, 2022.
- [38] David Ruhe, Jonathan Heek, Tim Salimans, and Emiel Hoogetboom. Rolling diffusion models. *arXiv preprint arXiv:2402.09470*, 2024.
- [39] Seyedmorteza Sadat, Otmar Hilliges, and Romann M Weber. Eliminating oversaturation and artifacts of high guidance scales in diffusion models. In *The Thirteenth International Conference on Learning Representations*.
- [40] Seyedmorteza Sadat, Jakob Buhmann, Derek Bradley, Otmar Hilliges, and Romann M. Weber. Cads: Unleashing the diversity of diffusion models through condition-annealed sampling. In *ICLR*, 2024. URL <https://openreview.net/forum?id=zMoNRajk2X>.
- [41] Seyedmorteza Sadat, Manuel Kansy, Otmar Hilliges, and Romann M Weber. No training, no problem: Rethinking classifier-free guidance for diffusion models. *arXiv preprint arXiv:2407.02687*, 2024.
- [42] Chitwan Saharia, William Chan, Saurabh Saxena, Lala Li, Jay Whang, Emily L Denton, Kamyar Ghasemipour, Raphael Gontijo Lopes, Burcu Karagol Ayan, Tim Salimans, et al. Photorealistic text-to-image diffusion models with deep language understanding. *Advances in neural information processing systems*, 35:36479–36494, 2022.

- [43] Tim Salimans and Jonathan Ho. Progressive distillation for fast sampling of diffusion models, 2022. URL <https://arxiv.org/abs/2202.00512>.
- [44] Jiahao Shao, Yuanbo Yang, Hongyu Zhou, Youmin Zhang, Yujun Shen, Matteo Poggi, and Yiyi Liao. Learning temporally consistent video depth from video diffusion priors. *arXiv preprint arXiv:2406.01493*, 2024.
- [45] Jascha Sohl-Dickstein, Eric A. Weiss, Niru Maheswaranathan, and Surya Ganguli. Deep unsupervised learning using nonequilibrium thermodynamics, 2015.
- [46] Yang Song, Jascha Sohl-Dickstein, Diederik P. Kingma, Abhishek Kumar, Stefano Ermon, and Ben Poole. Score-based generative modeling through stochastic differential equations, 2021.
- [47] George Stein, Jesse C. Cresswell, Rasa Hosseinzadeh, Yi Sui, Brendan Leigh Ross, Valentin Vilecroze, Zhaoyan Liu, Anthony L. Caterini, J. Eric T. Taylor, and Gabriel Loaiza-Ganem. Exposing flaws of generative model evaluation metrics and their unfair treatment of diffusion models, 2023. URL <https://arxiv.org/abs/2306.04675>.
- [48] Zhicong Tang, Jianmin Bao, Dong Chen, and Baining Guo. Diffusion models without classifier-free guidance. *arXiv preprint arXiv:2502.12154*, 2025.
- [49] Ulrike Von Luxburg and Bernhard Schölkopf. Statistical learning theory: Models, concepts, and results. In *Handbook of the History of Logic*, volume 10, pages 651–706. Elsevier, 2011.
- [50] Xi Wang, Nicolas Dufour, Nefeli Andreou, Marie-Paule Cani, Victoria Fernández Abrevaya, David Picard, and Vicky Kalogeiton. Analysis of classifier-free guidance weight schedulers. *arXiv preprint arXiv:2404.13040*, 2024.

## A Additional implementation details and experiments

**Constrast.** In Fig. 6, similar to saturation, we show that the discrepancy between M-SWG and other state-of-the-art methods is significant. The combination of competitive IS and FDD, with significantly less oversaturation and almost no overcontrast on average, suggests that samples remain relatively closer to the training data distribution. Contrast is computed as the root mean square contrast of the samples, meaning the standard deviation of intensities after greyscale conversion, similar to [36, 39].

**DiT: guidance scales w.r.t. Frechet distances.** Similar to [21], we have assumed that the generative error of  $\epsilon_{\text{pos}}$  can be primarily attributed to scaling factors, such as training time and number of parameters. In the main manuscript, we illustrate that the largest best-performing publicly available Unet architecture EDM2-XXL shows no improvement w.r.t. FID for SWG and only minimal improvement for reduced training (RT). However, this is not in line with DiT-XL/2. In Fig. 7, we demonstrate that the unguided generation can be significantly improved using SWG w.r.t. to both FID and FDD. We suspect that the observed discrepancy can be attributed to the significantly better inductive bias of EDM2-XXL, which leaves less room for improvement using guidance.

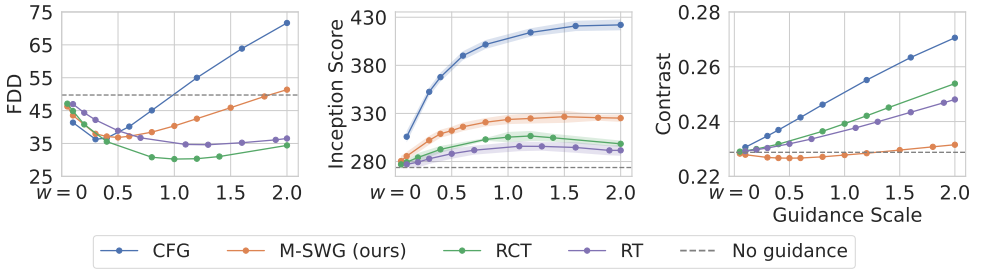


Figure 6: **Visualizing the achieved tradeoff by varying the guidance scale  $w$  (x-axis) for FDD (↓, left), Inception score (IS ↑, center), and contrast (↓, right) using EDM2-XXL. M-SWG does **not** exhibit undesired overcontrast compared to other state-of-the-art methods.**

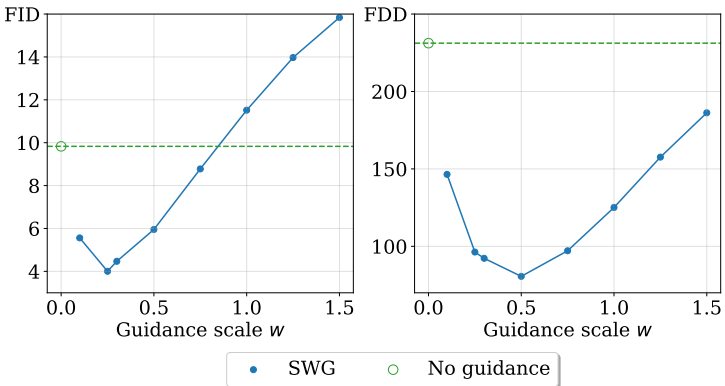


Figure 7: DiT-XL/2 on ImageNet 256x256. Frechet distances (y-axis) versus guidance scales (x-axis) using InceptionNetv3 (**FID**, left) and DINOv2 ViT-L (**FDD**, right).

**SWG implementation details and pseudocode.** To make SWG compatible with DiT, we add positional encoding interpolation on DiT-XL to process various resolutions. The choice of  $k \approx \frac{5}{8}H$  is determined by practical considerations of Unets. Specifically,  $k$  must satisfy  $\frac{k}{2^n} \in \mathbb{N}$ , where  $n$  is the number of downsampling steps of the Unet, and the diffusion model  $\boldsymbol{\epsilon}_{\text{pos}}$  must be able to process multiple image resolutions.

We provide an implementation of SWG in the Appendix A.

**Time overhead at sampling time.** In Appendix A, we present the time needed to produce 512 samples for various models and guidance methods and their corresponding estimate in images per second per GPU. We emphasize that we have naively implemented SWG, as shown in the pseudocode, and further optimization can help bridge the time overhead.

**Guidance interpolation.** Figs. 9 and 10 provide interpolations of guidance methods following

$$\tilde{\boldsymbol{\epsilon}}(\mathbf{x}, t) = \boldsymbol{\epsilon}_{\text{pos}}(\mathbf{x}, t) + \sum_i \alpha_i w_i [\boldsymbol{\epsilon}_{\text{pos}}(\mathbf{x}, t) - \boldsymbol{\epsilon}_{\text{neg}}^{(i)}(\mathbf{x}, t)] \quad (6)$$

where  $w_i$  are the optimized guidance scales w.r.t. FDD for each method and  $\alpha_i$  are set to form a convex combination between guidance terms.

Model/Res	Guidance	VRAM (GB) per GPU	Batch size	Time for 512 samples in minutes ( $\downarrow$ )	Estimate of Imgs/s per GPU ( $\uparrow$ )
EDM2-S 512 $\times$ 512	$\times$	15.2	256	1.36	12.54
	SWG ( $r=0.4$ )	15.2	256	2.10	8.12
	SWG ( $r=0$ )	15.2	256	1.85	9.22
	RT	15.2	256	1.77	9.64
	RCT	15.2	256	1.61	10.67
	CFG $^\dagger$	15.2	256	1.61	10.67
DiT-XL 256 $\times$ 256	$\times$	17.9	32	4.61	3.70
	CFG	17.9	32	8.45	2.02
	SWG	17.9	32	11.37	1.50

Table 6: All benchmarks were conducted using 2 Nvidia A100 GPUs with 40GB of VRAM. We benchmark sliding window guidance (SWG), classifier-free guidance (CFG), classifier-free guidance using a smaller capacity unconditional model (CFG $^\dagger$ ), reduced training (RT), and reduced capacity training (RCT). The symbol  $\times$  stands for *No guidance* ( $w = 0$ ). Crucially, SWG is implemented in a naive way with  $N = 4$  (as shown in the provided pseudocode) and can be further optimized, which is left to future work. The scalar  $r$  denotes the overlap ratio per dimension, where  $r = 0$  refers to no overlap.

	EDM			EDM2-S	
	CIFAR-10	CIFAR-100	FFHQ-64	ImageNet-512	
	FDD	FDD	FDD	FDD	FID
No Guidance	139.4	196.6	174.8	112.2	2.92
CFG [15]	99.9 <sub>0.6</sub>	126.6 <sub>0.6</sub>	–	52.9 <sub>0.8</sub> $^\dagger$	2.44 <sub>0.1</sub> $^\dagger$
<i>WMG methods</i>					
a) Reduced training	60.8 <sub>1.1</sub>	81.2 <sub>1.3</sub>	94.0 <sub>1.0</sub>	46.5 <sub>1.2</sub>	1.79 <sub>0.8</sub>
b) Reduced capacity	62.4 <sub>0.9</sub>	93.8 <sub>1.1</sub>	102.5 <sub>1.3</sub>	70.0 <sub>1.4</sub>	2.20 <sub>0.7</sub>
c) RCT (a + b)	62.1 <sub>0.8</sub>	87.0 <sub>1.0</sub>	95.3 <sub>1.0</sub>	<b>42.1<sub>1.4</sub></b>	<b>1.67<sub>0.8</sub></b>
d) Weight decay fine-tuning	65.0 <sub>1.3</sub>	88.1 <sub>1.4</sub>	111.2 <sub>2.4</sub>	52.1 <sub>0.6</sub>	2.46 <sub>0.1</sub>
e) Weight decay + (a)	<b>59.0<sub>0.9</sub></b>	<b>75.9<sub>1.1</sub></b>	<b>92.6<sub>1.0</sub></b>	43.9 <sub>0.9</sub>	2.25 <sub>0.2</sub>
f) Weight decay re-training	64.7 <sub>1.3</sub>	93.3 <sub>1.3</sub>	133.0 <sub>1.4</sub>	–	–

Table 7: Extension of Table 5 (main text) with EDM [22]. FDD ( $\downarrow$ ) and FID ( $\downarrow$ ), with the guidance weight in subscript. FFHQ-64 is the only unconditional task; all other experiments used class labels as model conditions for both networks.  $^\dagger$  The negative model additionally has reduced capacity (EDM2-XS).

Settings	EDM2-S, ImageNet-512							
	FDD				FID			
	$c_{\text{pos}}$	$c_{\text{neg}}$	Size	$\lambda$	$c_{\text{pos}}$	$c_{\text{neg}}$	Size	$\lambda$
No guidance	2147	2147	S	0	2147	2147	S	0
CFG <sup>†</sup>	2147	2147	S	0	2147	2147	S	0
<i>WMG methods</i>								
a) Reduced training	2147	67	S	0	2147	134	S	0
b) Reduced capacity	2147	2147	XS	0	2147	2147	XS	0
c) RCT (a + b)	2147	134	XS	0	2147	268	XS	0
d) Weight decay fine-tuning	2147	2233	S	2e-5	2147	2243	S	2e-5
e) Weight decay + (a)	2147	63	S	2e-5	2147	63	S	2e-5

Table 8: Settings for Table 5 (main text) on ImageNet-512 using EDM2-S. **Columns** specify the checkpoint of the positive model  $c_{\text{pos}}$  in million images seen, the checkpoint of the negative model  $c_{\text{neg}}$  in million images seen, the model size (EDM2 variants), and the weight decay parameter  $\lambda$ .

Settings	EDM											
	CIFAR-10				CIFAR-100				FFHQ-64			
	$c_{\text{pos}}$	$c_{\text{neg}}$	Size	$\lambda$	$c_{\text{pos}}$	$c_{\text{neg}}$	Size	$\lambda$	$c_{\text{pos}}$	$c_{\text{neg}}$	Size	$\lambda$
No guidance	500	500	F	0	500	500	F	0	500	500	F	0
CFG	500	500	F	0	500	500	F	0	500	500	F	0
<i>WMG methods</i>												
a) Reduced training	500	20	F	0	500	20	F	0	500	20	F	0
b) Reduced capacity	500	500	S	0	500	500	S	0	500	500	S	0
c) RCT (a + b)	500	200	S	0	500	100	S	0	500	100	S	0
d) WD fine-tuning	500	560	F	5e-4	500	520	F	5e-4	500	540	F	2e-3
e) WD and reduced training	500	30	F	5e-4	500	20	F	5e-4	500	20	F	2e-3
f) WD re-training	500	500	F	5e-4	500	500	F	5e-4	500	500	F	2e-3

Table 9: Settings for Table 7 on small-scale benchmarks using EDM. On CIFAR-10, CIFAR-100, and FFHQ-64. CFG uses an unconditional but otherwise identical model to the positive model as a negative model. **Columns** specify the checkpoint of the positive model  $c_{\text{pos}}$  in million images seen, the checkpoint of the negative model  $c_{\text{neg}}$  in million images seen, the model size (F for full and S for small), and the weight decay parameter  $\lambda$ . The full model corresponds to the default architecture hyperparameter settings as detailed in [22]. The small model has a reduced number of resolution levels and channel size (cres=1,1 for CIFAR-10 / CIFAR-100 and cres=1,1,1 for FFHQ) and a reduced number of blocks per level (num\_blocks=2 for CIFAR-10 / CIFAR-100).

```

1 import torch
2
3 def SWG(x, e_pos, t, labels, N, k, w):
4     # x: noisy images of size [bs, c, H, H]
5     # e_pos: network i.e. Unet
6     # t: timestep
7     # labels: class conditions
8     # N: number of crops in [4,9,16,...]
9     # k: crop size
10    # w: guidance scale
11
12    steps_per_dim = int(torch.sqrt(N))
13    y_pos = e_pos(x, t, labels)
14    bs, c, H, _ = x.shape
15    y_neg = torch.zeros_like(x)
16    overlap = torch.zeros_like(x)
17    stride = (H - k) // (steps_per_dim - 1)
18    for i in range(steps_per_dim):
19        for j in range(steps_per_dim):
20            # left edge (le), right edge (re)
21            le, re = stride * i, stride * i + k
22            # top edge (te), bottom edge (be)
23            te, be = stride * j, stride * j + k
24            # x_p is of shape [bc, c, k, k]
25            x_p = x[:, :, te:be, le:re]
26            y_crop = e_pos(x_p, t, labels)
27            y_neg[:, :, te:be, le:re] += y_crop
28            o_p = torch.ones_like(y_crop)
29            overlap[:, :, te:be, le:re] += o_p
30    # pixel averaging
31    y_neg = y_neg / overlap
32    # Equation 2 in the main text
33    return y_pos + w * (y_pos - y_neg)
34

```

Figure 8: Example pseudocode for sliding window guidance (SWG) in Python using the torch library.

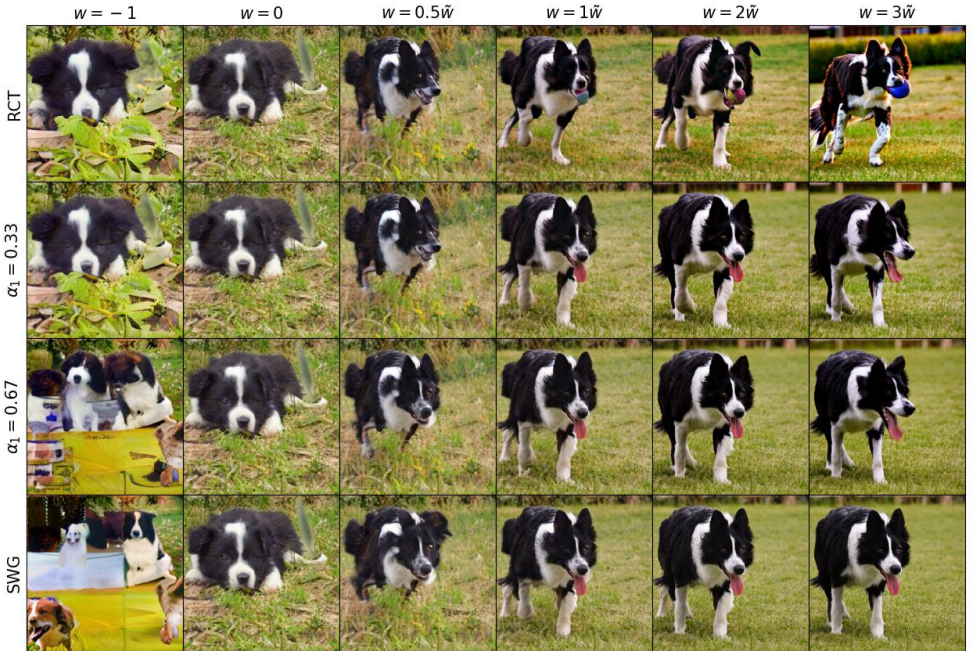


Figure 9: Samples generated by interpolating RCT and SWG with different guidance weights, but the same initial noise. The noise predictor  $\epsilon_{pos}$  is based on the EDM2-XXL network trained on ImageNet-512. **Columns from left to right:** guidance weights  $w$  are scaled by  $\tilde{w}$ , with  $\tilde{w}$  the individual weight for each method corresponding to the lowest FDD ( $\tilde{w} = 1$  for RCT and  $\tilde{w} = 0.2$  for SWG). The first column shows samples using  $\epsilon_{neg}$  as a noise predictor ( $w = -1$ ). Interpolations are computed according to Equation (6) with a convex combination of the guidance terms parametrized by  $\alpha_1$  and  $\alpha_2 = 1 - \alpha_1$ .

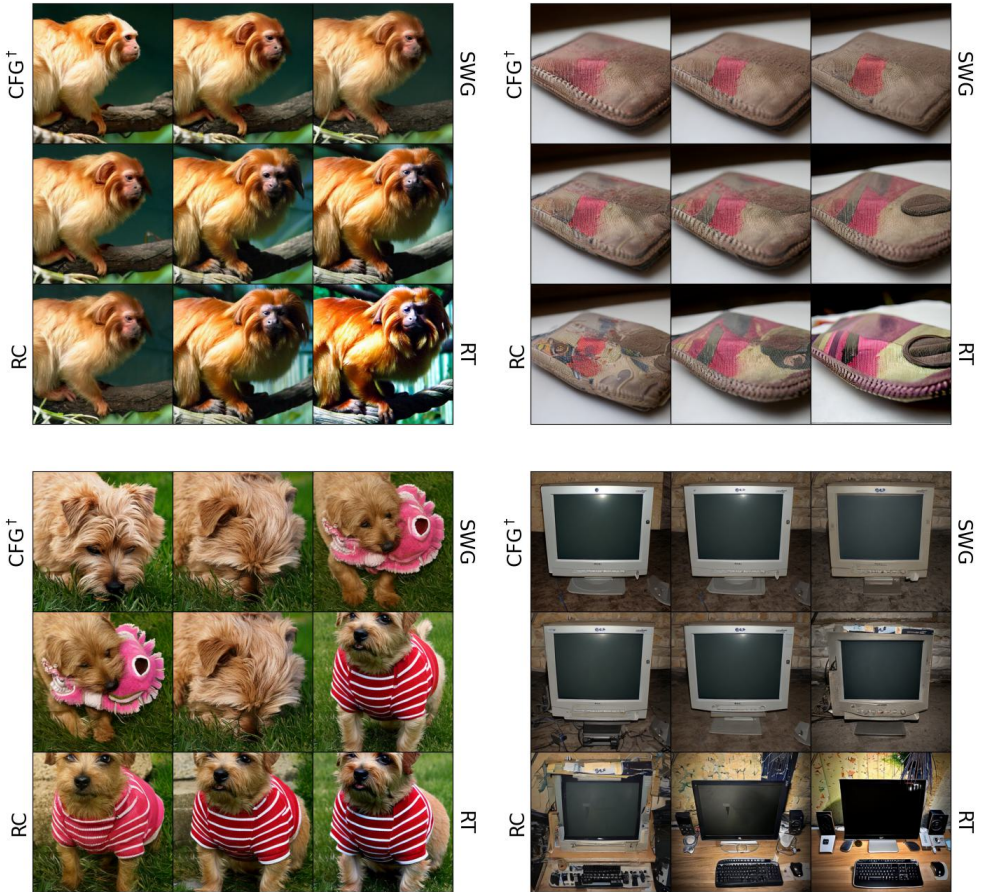


Figure 10: Samples generated by interpolating CFG, SWG, RC (reduced capacity), and RT (reduced training) with different guidance weights but the same initial noise. The noise predictor  $\epsilon_{pos}$  is based on the EDM2-XXL network trained on ImageNet-512. Respective weights are CFG:  $w = 0.6$ , SWG:  $w = 0.2$ , RT:  $w = 1.0$  and RC:  $w = 1.0$ . Interpolations are computed according to Equation (6), such that the sum over guidance terms is a convex combination, with  $\alpha_i = 1$  in the corners and linear interpolation in between.

## B Toy example details

This section presents the derivation of the toy example from the main text. The code for computing the trajectories will be released and allows for the visualization of guidance effects for different combinations of  $\boldsymbol{\epsilon}_{\text{pos}}$ ,  $\boldsymbol{\epsilon}_{\text{neg}}$ , and datasets. We introduce with time  $t \in [0, 1]$  a variable that denotes the progress of denoising, which starts from a normally distributed sample,  $\mathbf{x}(1)$ , and ends at a fully denoised sample,  $\mathbf{x}(0)$ . In the following, we denote by  $\mathbf{y}$  a sample from the data distribution  $P(\mathbf{y})$ , by  $\sigma := \sigma(t)$  the time-dependent noise level, and by  $\mathbf{x} := \mathbf{x}(t)$  a point along a denoising trajectory. We set  $\sigma(0) = 0$  and choose with  $\sigma(1) = 80$  a value such that  $\sigma(t) \gg \text{std}(y_i)$ , for all dimensions  $i \in \{1, 2, \dots, d\}$ . We assume  $\sigma(t)$  to be a strictly monotone increasing function in time  $t$ . To derive the optimal denoiser, we make use of the ordinary differential equation (ODE) that describes the field lines of probability flow (e.g. Eq. (1) of Ref. [22]). This ODE allows for the generation of sampling trajectories

$$d\mathbf{x} = -\dot{\sigma}\nabla_{\mathbf{x}}\log P(\mathbf{x}|\sigma^2)dt, \quad (7)$$

when initialized with a noise sample  $\mathbf{x}(1) \sim \mathcal{N}(\mathbf{x}|0, \sigma(1)^2)$ . Here and in following we use the definition  $\mathcal{N}(\mathbf{x}|\boldsymbol{\mu}, \sigma^2) := \mathcal{N}(\mathbf{x}|\boldsymbol{\mu}, \sigma^2 I_d)$  to denote an isotropic normal distribution. Note that  $dt < 0$  for inference, by definition. Furthermore,  $\dot{\sigma}\sigma$  can be interpreted as a diffusion coefficient,  $\nabla_{\mathbf{x}}\log P(\mathbf{x}|\sigma^2)$  as a score function, and  $P(\mathbf{x}|\sigma^2) = \int_{\mathbb{R}^d} \mathcal{N}(\mathbf{x}|\mathbf{y}, \sigma^2)P(\mathbf{y})d\mathbf{y}$  as the distribution of noisy samples, which results from adding Gaussian noise to data samples. To derive the optimal denoiser, we rewrite the score function as

$$\begin{aligned} -\nabla_{\mathbf{x}}\log P(\mathbf{x}|\sigma^2) &= -\frac{\nabla_{\mathbf{x}}P(\mathbf{x}|\sigma^2)}{P(\mathbf{x}|\sigma^2)} \\ &= -\frac{\nabla_{\mathbf{x}}\int_{\mathbb{R}^d}\mathcal{N}(\mathbf{x}|\mathbf{y}, \sigma^2)P(\mathbf{y})d\mathbf{y}}{P(\mathbf{x}|\sigma^2)} \\ &= \frac{\int_{\mathbb{R}^d}\frac{\mathbf{x}-\mathbf{y}}{\sigma^2}\mathcal{N}(\mathbf{x}|\mathbf{y}, \sigma^2)P(\mathbf{y})d\mathbf{y}}{P(\mathbf{x}|\sigma^2)} \\ &= \frac{1}{\sigma^2}\int_{\mathbb{R}^d}(\mathbf{x}-\mathbf{y})P(\mathbf{y}|\mathbf{x}, \sigma^2)d\mathbf{y} \\ &= \frac{1}{\sigma^2}\left(\int_{\mathbb{R}^d}\mathbf{x}P(\mathbf{y}|\mathbf{x}, \sigma^2)d\mathbf{y}-\int_{\mathbb{R}^d}\mathbf{y}P(\mathbf{y}|\mathbf{x}, \sigma^2)d\mathbf{y}\right) \\ &= \frac{\mathbf{x}-\mathbf{y}^*(\mathbf{x}, \sigma)}{\sigma^2}, \end{aligned} \quad (8)$$

where the optimal denoiser is given by the posterior mean

$$\mathbf{y}^*(\mathbf{x}, \sigma) := \int_{\mathbb{R}^d}\mathbf{y}P(\mathbf{y}|\mathbf{x}, \sigma^2)d\mathbf{y} = \int_{\mathbb{R}^d}\mathbf{y}\frac{\mathcal{N}(\mathbf{x}|\mathbf{y}, \sigma^2)P(\mathbf{y})}{P(\mathbf{x}|\sigma^2)}d\mathbf{y}. \quad (9)$$

To construct an error-prone denoiser, we substitute the true data distribution with a ‘‘broader’’ data distribution  $P(\mathbf{y}) \rightarrow P_{\delta}(\mathbf{y})$ , with  $P_{\delta}(\mathbf{y}) = \int_{\mathbb{R}^d}\mathcal{N}(\mathbf{y}|\mathbf{y}', \delta^2)P(\mathbf{y}')d\mathbf{y}'$ , where  $\delta$  is the standard deviation of noise that randomly shifts the true data points. The corresponding posterior mean is given by

$$\begin{aligned} \mathbf{y}_{\delta}(\mathbf{x}, \sigma) &:= \int_{\mathbb{R}^d}\mathbf{y}\frac{\mathcal{N}(\mathbf{x}|\mathbf{y}, \sigma^2)P_{\delta}(\mathbf{y})}{P_{\delta}(\mathbf{x}|\sigma^2)}d\mathbf{y} \\ &= \frac{\int_{\mathbb{R}^d}\int_{\mathbb{R}^d}\mathbf{y}\mathcal{N}(\mathbf{x}|\mathbf{y}, \sigma^2)\mathcal{N}(\mathbf{y}|\mathbf{y}', \delta^2)P(\mathbf{y}')d\mathbf{y}'d\mathbf{y}}{\int_{\mathbb{R}^d}\int_{\mathbb{R}^d}\mathcal{N}(\mathbf{x}|\mathbf{y}, \sigma^2)\mathcal{N}(\mathbf{y}|\mathbf{y}', \delta^2)P(\mathbf{y}')d\mathbf{y}'d\mathbf{y}}, \end{aligned} \quad (10)$$

with  $P_\delta(\mathbf{x}|\sigma^2) := \int_{\mathbb{R}^d} \mathcal{N}(\mathbf{x}|\mathbf{y}, \sigma^2) P_\delta(\mathbf{y}) d\mathbf{y}$ . To find an explicit expression for  $\mathbf{y}_\delta$ , we utilize known integrals [63]. For the denominator, we use the expression

$$\int_{\mathbb{R}^d} \phi(\mathbf{x}) \phi(\mathbf{a} + b\mathbf{x}) d\mathbf{x} = \frac{1}{\sqrt{1+b^2}} \phi\left(\frac{\mathbf{a}}{\sqrt{1+b^2}}\right). \quad (11)$$

with  $\phi(\mathbf{x}) := \mathcal{N}(\mathbf{x}|0, 1)$ . However, we have to reformulate this expression for the product of two Gaussians with different means and variances. To this end, consider the substitution  $\mathbf{x} = \frac{\mathbf{z}-\mathbf{c}}{d}$ ,  $c, d \in \mathbb{R}$  and adjust the LHS.

$$\begin{aligned} \int_{\mathbb{R}^d} \phi(\mathbf{x}) \phi(\mathbf{a} + b\mathbf{x}) d\mathbf{x} &= \int_{\mathbb{R}^d} \phi\left(\frac{\mathbf{z}-\mathbf{c}}{d}\right) \phi\left(\mathbf{a} + b\frac{\mathbf{z}-\mathbf{c}}{d}\right) \frac{1}{d} d\mathbf{z} \\ &= \int_{\mathbb{R}^d} \phi\left(\frac{\mathbf{z}-\mathbf{c}}{d}\right) \phi\left(\frac{\mathbf{z}-\boldsymbol{\mu}}{\sigma}\right) \frac{1}{d} d\mathbf{z} \quad , \quad \boldsymbol{\mu} = \mathbf{c} - \mathbf{a}\frac{d}{b}, \sigma = \frac{d}{b} \\ &= \sigma \int_{\mathbb{R}^d} \mathcal{N}(\mathbf{z}|\mathbf{c}, d^2) \mathcal{N}(\mathbf{z}|\boldsymbol{\mu}, \sigma^2) d\mathbf{z}. \end{aligned}$$

Combining with the RHS of Equation (11) yields the desired integration formula

$$\begin{aligned} \int_{\mathbb{R}^d} \mathcal{N}(\mathbf{z}|\mathbf{c}, d^2) \mathcal{N}(\mathbf{z}|\boldsymbol{\mu}, \sigma^2) d\mathbf{z} &= \frac{1}{\sigma} \frac{1}{\sqrt{1+b^2}} \phi\left(\frac{\mathbf{a}}{\sqrt{1+b^2}}\right) \\ &= \frac{1}{\sqrt{\sigma^2+d^2}} \phi\left(\frac{\mathbf{c}-\boldsymbol{\mu}}{\sqrt{\sigma^2+d^2}}\right) = \mathcal{N}(\mathbf{c}|\boldsymbol{\mu}, \sigma^2+d^2). \end{aligned} \quad (12)$$

For the numerator, we use the expression [63]

$$\int_{\mathbb{R}^d} \mathbf{x} \phi(\mathbf{x}) \phi(\mathbf{a} + b\mathbf{x}) d\mathbf{x} = -\frac{ab}{(1+b^2)^{\frac{3}{2}}} \phi\left(\frac{\mathbf{a}}{\sqrt{1+b^2}}\right). \quad (13)$$

Using the same substitutions as before yields

$$\begin{aligned} &\int_{\mathbb{R}^d} \mathbf{x} \phi(\mathbf{x}) \phi(\mathbf{a} + b\mathbf{x}) d\mathbf{x} \\ &= \int_{\mathbb{R}^d} \frac{\mathbf{z}-\mathbf{c}}{d} \phi\left(\frac{\mathbf{z}-\mathbf{c}}{d}\right) \phi\left(\frac{\mathbf{z}-\boldsymbol{\mu}}{\sigma}\right) \frac{1}{d} d\mathbf{z} \\ &= \frac{1}{d} \int_{\mathbb{R}^d} \mathbf{z} \sigma \mathcal{N}(\mathbf{z}|\mathbf{c}, d^2) \mathcal{N}(\mathbf{z}|\boldsymbol{\mu}, \sigma^2) d\mathbf{z} - \frac{c}{d} \int_{\mathbb{R}^d} \mathcal{N}(\mathbf{z}|\mathbf{c}, d^2) \mathcal{N}(\mathbf{z}|\boldsymbol{\mu}, \sigma^2) d\mathbf{z} \\ &\stackrel{(12)}{=} \frac{1}{d} \int_{\mathbb{R}^d} \mathbf{z} \sigma \mathcal{N}(\mathbf{z}|\mathbf{c}, d^2) \mathcal{N}(\mathbf{z}|\boldsymbol{\mu}, \sigma^2) d\mathbf{z} - \frac{c}{d} \mathcal{N}(\mathbf{c}|\boldsymbol{\mu}, \sigma^2+d^2). \end{aligned}$$

Combining with the RHS of Equation (13) yields the second integration formula

$$\begin{aligned}
& \int_{\mathbb{R}^d} \mathbf{z} \sigma \mathcal{N}(\mathbf{z}|\mathbf{c}, d^2) \mathcal{N}(\mathbf{z}|\boldsymbol{\mu}, \sigma^2) d\mathbf{z} \tag{14} \\
&= \frac{d}{\sigma} \left( -\frac{\mathbf{c} - \boldsymbol{\mu}}{\sigma} \frac{d}{\sigma} \left( \frac{\sigma}{\sqrt{\sigma^2 + d^2}} \right)^3 \phi \left( \frac{\mathbf{c} - \boldsymbol{\mu}}{\sqrt{\sigma^2 + d^2}} \right) + \frac{\sigma \mathbf{c}}{d} \mathcal{N}(\mathbf{c}|\boldsymbol{\mu}, \sigma^2 + d^2) \right) \\
&= \frac{d}{\sigma} \left( -\frac{(\mathbf{c} - \boldsymbol{\mu})d}{\sigma^2} \frac{\sigma^3}{\sigma^2 + d^2} \mathcal{N}(\mathbf{c}|\boldsymbol{\mu}, \sigma^2 + d^2) + \frac{\sigma \mathbf{c}}{d} \mathcal{N}(\mathbf{c}|\boldsymbol{\mu}, \sigma^2 + d^2) \right) \\
&= \mathcal{N}(\mathbf{c}|\boldsymbol{\mu}, \sigma^2 + d^2) \left( \mathbf{c} - \frac{(\mathbf{c} - \boldsymbol{\mu})d^2}{\sigma^2 + d^2} \right) \\
&= \mathcal{N}(\mathbf{c}|\boldsymbol{\mu}, \sigma^2 + d^2) \frac{\mathbf{c}\sigma^2 + \boldsymbol{\mu}d^2}{\sigma^2 + d^2}. \tag{15}
\end{aligned}$$

For the numerator, of Eq. (10) we now get

$$\begin{aligned}
& \int_{\mathbb{R}^d} \mathbf{y} \mathcal{N}(\mathbf{x}|\mathbf{y}, \sigma^2) \int_{\mathbb{R}^d} \mathcal{N}(\mathbf{y}|\mathbf{y}', \delta^2) P(\mathbf{y}') d\mathbf{y}' d\mathbf{y} \tag{16} \\
&= \int_{\mathbb{R}^d} \int_{\mathbb{R}^d} \mathbf{y} \mathcal{N}(\mathbf{y}|\mathbf{x}, \sigma^2) \mathcal{N}(\mathbf{y}|\mathbf{y}', \delta^2) d\mathbf{y} P(\mathbf{y}') d\mathbf{y}' \\
&\stackrel{(14)}{=} \int_{\mathbb{R}^d} \mathcal{N}(\mathbf{x}|\mathbf{y}', \sigma^2 + \delta^2) \frac{\mathbf{x}\delta^2 + \mathbf{y}'\sigma^2}{\sigma^2 + \delta^2} P(\mathbf{y}') d\mathbf{y}' \\
&= \frac{1}{\sigma^2 + \delta^2} \int_{\mathbb{R}^d} (\mathbf{x}\delta^2 + \mathbf{y}'\sigma^2) P(\mathbf{x}, \mathbf{y}'|\sigma^2 + \delta^2) d\mathbf{y}'. \tag{17}
\end{aligned}$$

For the denominator of Eq. (10), we get

$$\begin{aligned}
P_\delta(\mathbf{x}|\sigma^2) &= \int_{\mathbb{R}^d} \mathcal{N}(\mathbf{x}|\mathbf{y}, \sigma^2) P_\delta(\mathbf{y}) d\mathbf{y} \\
&= \int_{\mathbb{R}^d} \mathcal{N}(\mathbf{x}|\mathbf{y}, \sigma^2) \int_{\mathbb{R}^d} \mathcal{N}(\mathbf{y}|\mathbf{y}', \delta^2) P(\mathbf{y}') d\mathbf{y}' d\mathbf{y} \\
&= \int_{\mathbb{R}^d} \int_{\mathbb{R}^d} \mathcal{N}(\mathbf{y}|\mathbf{x}, \sigma^2) \mathcal{N}(\mathbf{y}|\mathbf{y}', \delta^2) d\mathbf{y} P(\mathbf{y}') d\mathbf{y}' \\
&\stackrel{(12)}{=} \int_{\mathbb{R}^d} \mathcal{N}(\mathbf{x}|\mathbf{y}', \sigma^2 + \delta^2) P(\mathbf{y}') d\mathbf{y}' \\
&= \int_{\mathbb{R}^d} \mathcal{N}(\mathbf{x}|\mathbf{y}', \sigma^2 + \delta^2) P(\mathbf{y}') d\mathbf{y}' \\
&= P(\mathbf{x}|\sigma^2 + \delta^2). \tag{18}
\end{aligned}$$

Finally,

$$\begin{aligned}
\mathbf{y}_\delta(\mathbf{x}, \sigma) &\stackrel{(16)+(18)}{=} \frac{\int_{\mathbb{R}^d} (\mathbf{x}\delta^2 + \mathbf{y}'\sigma^2) P(\mathbf{x}, \mathbf{y}'|\tilde{\sigma}^2) d\mathbf{y}'}{P(\mathbf{x}|\tilde{\sigma}^2)} \frac{1}{\tilde{\sigma}^2} \\
&= \frac{\mathbf{x}\delta^2 \int_{\mathbb{R}^d} P(\mathbf{x}, \mathbf{y}'|\tilde{\sigma}^2) d\mathbf{y}' + \sigma^2 \int_{\mathbb{R}^d} \mathbf{y}' P(\mathbf{x}, \mathbf{y}'|\tilde{\sigma}^2) d\mathbf{y}'}{P(\mathbf{x}|\tilde{\sigma}^2)} \frac{1}{\tilde{\sigma}^2} \\
&= \frac{\mathbf{x}\delta^2 + \sigma^2 \int_{\mathbb{R}^d} \mathbf{y}' \frac{P(\mathbf{x}, \mathbf{y}'|\tilde{\sigma}^2)}{P(\mathbf{x}|\tilde{\sigma}^2)} d\mathbf{y}'}{\tilde{\sigma}^2} \\
&= \frac{\mathbf{x}\delta^2 + \mathbf{y}^*(\mathbf{x}, \tilde{\sigma})\sigma^2}{\tilde{\sigma}^2}. \tag{19}
\end{aligned}$$

with  $\tilde{\sigma}^2 = \sigma^2 + \delta^2$ . Using the optimal denoiser  $\mathbf{y}^*$ , we define the optimal noise predictor

$$\boldsymbol{\varepsilon}^*(\mathbf{x}, \sigma) := -\sigma \nabla_{\mathbf{x}} \log P(\mathbf{x} | \sigma^2) \stackrel{(8)}{=} \frac{\mathbf{x} - \mathbf{y}^*(\mathbf{x}, \sigma)}{\sigma}, \quad (20)$$

and similarly, we define the error-prone noise predictor as

$$\boldsymbol{\varepsilon}_{err}(\mathbf{x}, \sigma) := \frac{\mathbf{x} - \mathbf{y}_{\delta}(\mathbf{x}, \sigma)}{\sigma}. \quad (21)$$

Inserting the explicit expression for  $\mathbf{y}_{\delta}$  in Equation (21) yields the expression for  $\boldsymbol{\varepsilon}_{err}$  used in the main text

$$\boldsymbol{\varepsilon}_{err}(\mathbf{x}, \sigma) = \frac{\mathbf{x} - \mathbf{y}_{\delta}(\mathbf{x}, \sigma)}{\sigma} = \frac{\mathbf{x} - \frac{\mathbf{x}\delta^2 + \mathbf{y}^*(\mathbf{x}, \tilde{\sigma})\sigma^2}{\tilde{\sigma}^2}}{\sigma} = \frac{1}{\sigma} \frac{\sigma^2(\mathbf{x} - \mathbf{y}^*(\mathbf{x}, \tilde{\sigma}))}{\tilde{\sigma}^2} = \frac{\sigma}{\tilde{\sigma}} \boldsymbol{\varepsilon}^*(\mathbf{x}, \tilde{\sigma}).$$

We can now generate trajectories  $\mathbf{x}(t)$  from Equation (7) by numerically solving the ODE with  $\mathbf{y}^*$  or  $\mathbf{y}_{\delta}$ , corresponding to  $\boldsymbol{\varepsilon}^*$  or  $\boldsymbol{\varepsilon}_{err}$ . In practice, we consider a finite set of data-points  $\{\mathbf{y}_i\}_{i=1}^N$ , in which case Equation (9) and Equation (19) simplify to

$$\mathbf{y}^*(\mathbf{x}, \sigma) = \frac{\sum_i \mathbf{y}_i N(\mathbf{x}(t) | \mathbf{y}_i, \sigma^2)}{\sum_i N(\mathbf{x}(t) | \mathbf{y}_i, \sigma^2)} \quad (22)$$

$$\mathbf{y}_{\delta}(\mathbf{x}, \sigma) = \frac{\mathbf{x}\delta^2 + \mathbf{y}^*(\mathbf{x}, \tilde{\sigma})\sigma^2}{\tilde{\sigma}^2}, \quad (23)$$

which can be directly used to simulate trajectories. To do so, we use the Euler method shown in Algorithm 1. We found that higher-order integration methods (e.g., Alg. 1 of Ref. [2]) can be used but are not necessary to achieve sufficient accuracy. This framework can be used for simulations of different configurations of  $\boldsymbol{\varepsilon}^*$ ,  $\boldsymbol{\varepsilon}_{err}$ , conditional and unconditional models, as well as arbitrary finite datasets in  $\mathbb{R}^n$ . Figs. 12 and 13 show a detailed analysis of WMG on two datasets, the triangle formation used in the main text, and a cloud of normally distributed data samples.

---

#### Algorithm 1 Euler method

---

**Require:** positive denoiser  $\mathbf{y}_{\delta}$ , negative denoiser  $\mathbf{y}_{\delta'}$ , guidance weight  $w(\mathbf{x}, \sigma)$ ,  $t_i \in \{0, \dots, N\} \in [0, 1]$

**sample**  $x_0 \sim \mathcal{N}(\mathbf{x} | 0, \sigma(1)^2 I_d)$

**for**  $i$  in  $0, \dots, N-1$  **do**

$\sigma_i, \sigma_{i+1} = \sigma(t_i), \sigma(t_{i+1})$

▷ Set current and next noise level

$\tilde{\mathbf{y}}_i = \mathbf{y}_{\delta}(\mathbf{x}_i, \sigma_i^2) + w(\mathbf{x}, \sigma_i)[\mathbf{y}_{\delta}(\mathbf{x}_i, \sigma_i^2) - \mathbf{y}_{\delta'}(\mathbf{x}_i, \sigma_i^2)]$

▷ Compute guidance target

**prediction**

$\mathbf{d}_i = (\mathbf{x}_i - \tilde{\mathbf{y}}_i) / \sigma_i$

▷ Compute score

$\mathbf{x}_{i+1} = \mathbf{x}_i + (\sigma_{i+1} - \sigma_i) \mathbf{d}_i$

▷ Update the trajectory

---

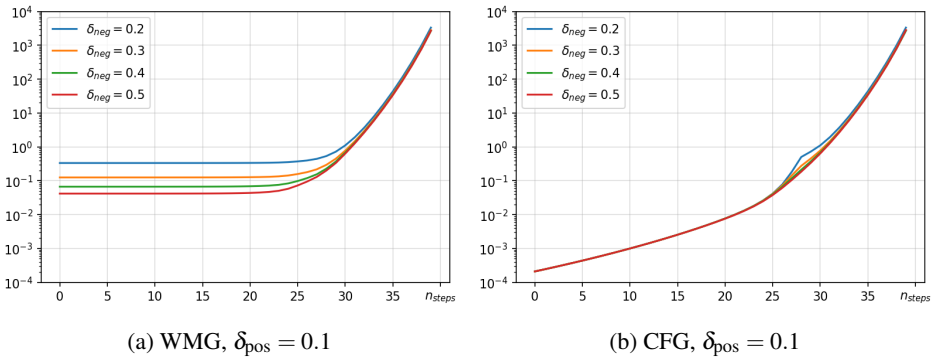


Figure 11: Optimal guidance weight for WMG and CFG in a toy example simulation. The  $x$ -axis shows the sampling step and the  $y$ -axis the guidance weight value, averaged over 100 trajectories with random initialization. The dataset and models  $\boldsymbol{\epsilon}_{\text{pos}}$  and  $\boldsymbol{\epsilon}_{\text{neg}}$  are as described in the main text. For both guidance methods,  $\boldsymbol{\epsilon}_{\text{pos}}$  has a variance of  $\delta_{\text{pos}} = 0.1$  and different values for  $\delta_{\text{neg}}$  are shown.

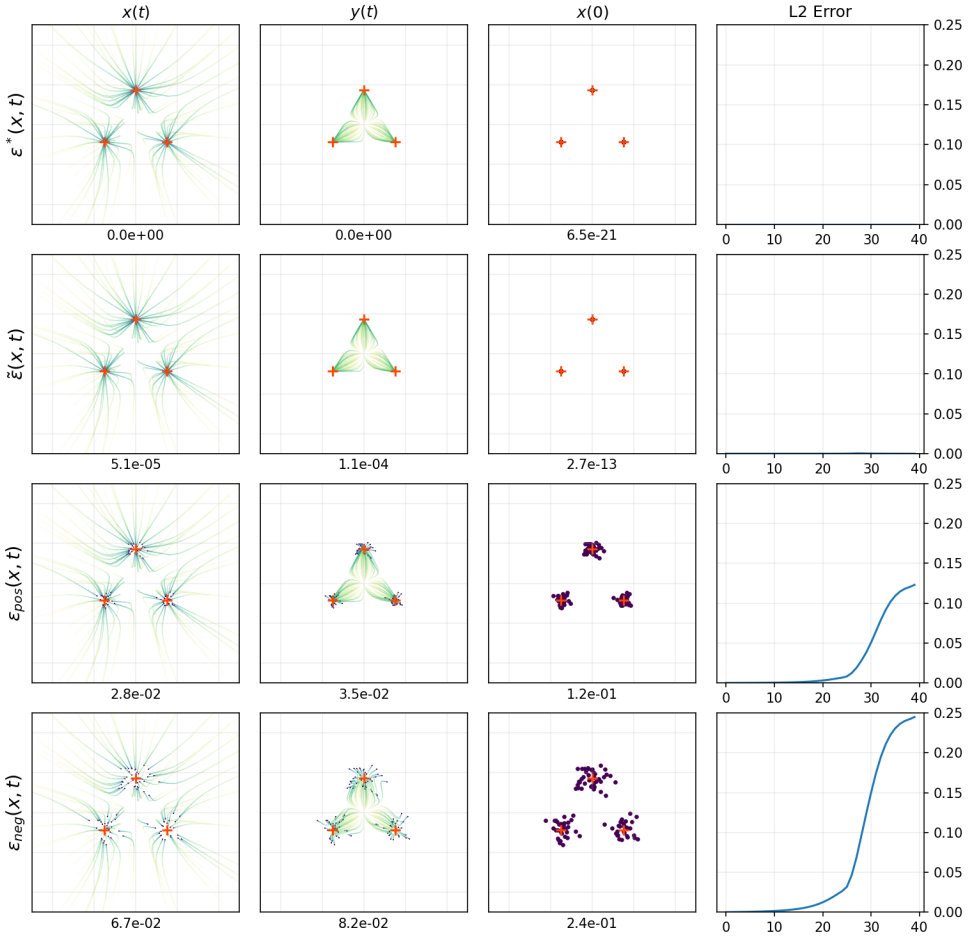


Figure 12: Toy example simulation for WMG with optimal guidance weight  $w^*(\mathbf{x}, t)$  for three equidistant data points, using 40 sampling steps. **Columns from left to right:** The trajectory  $\mathbf{x}(t)$ , the target prediction  $\mathbf{y}(t)$ , the trajectory endpoints  $\mathbf{x}(1)$ , and the average step-wise L2 error to the optimal noise predictor  $\boldsymbol{\epsilon}^*$  along the trajectory. The numbers below the plots in the first three columns show the average L2 error to the optimal trajectory (additionally averaged over steps for  $\mathbf{x}(t)$  and  $\mathbf{y}(t)$ ). **Rows from top to bottom:** The optimal noise predictor  $\boldsymbol{\epsilon}^*$ , the WMG noise predictor  $\tilde{\boldsymbol{\epsilon}} = \boldsymbol{\epsilon}_{\text{pos}} + w[\boldsymbol{\epsilon}_{\text{pos}} - \boldsymbol{\epsilon}_{\text{neg}}]$  with optimal weight  $w^*(\mathbf{x}, t)$ ,  $\boldsymbol{\epsilon}_{\text{pos}}$  ( $w = 0$ ), and  $\boldsymbol{\epsilon}_{\text{neg}}$  ( $w = -1$ ).

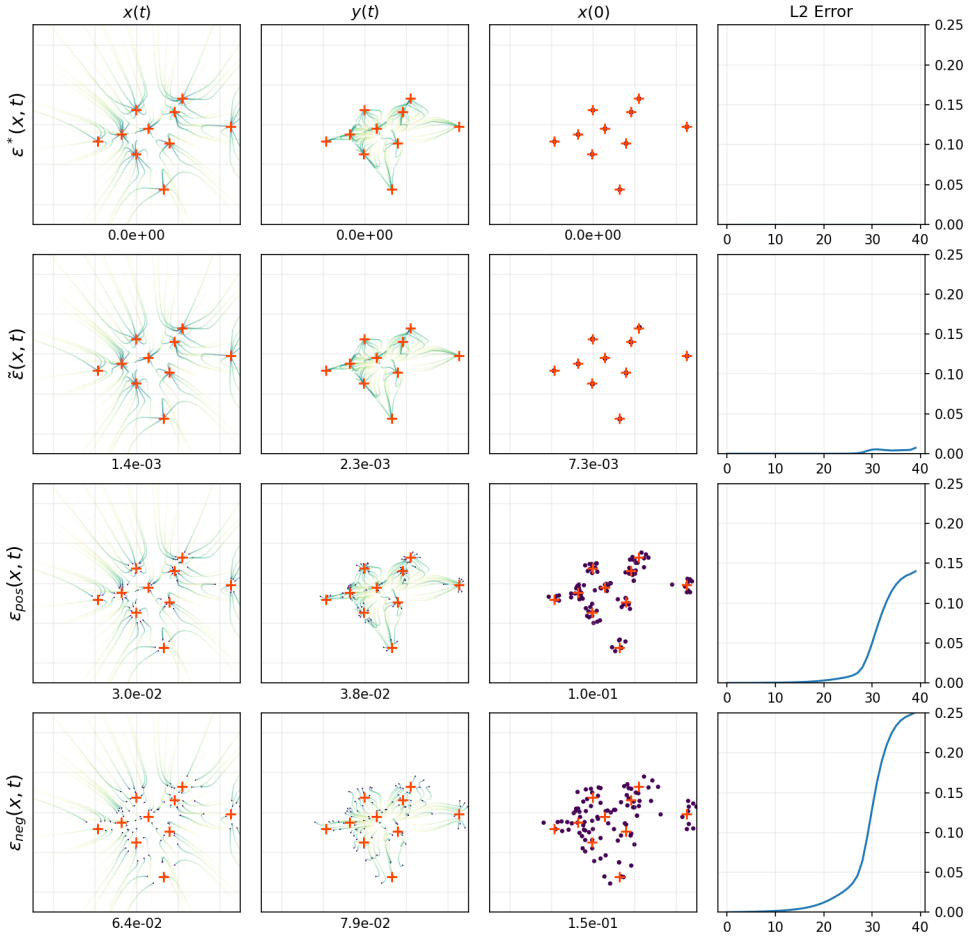


Figure 13: Toy example simulations for WMG with optimal guidance weight  $w^*(\mathbf{x}, t)$  for cloud of normally distributed data points, using 40 sampling steps. **Columns from left to right:** The trajectory  $\mathbf{x}(t)$ , the target prediction  $\mathbf{y}(t)$ , the trajectory endpoints  $\mathbf{x}(1)$ , and the average step-wise L2 error to the optimal noise predictor  $\boldsymbol{\varepsilon}^*$  along the trajectory. The numbers below the plots in the first three columns show the average L2 error to the optimal trajectory (additionally averaged over steps for  $\mathbf{x}(t)$  and  $\mathbf{y}(t)$ ). **Rows from top to bottom:** The optimal noise predictor  $\boldsymbol{\varepsilon}^*$ , the WMG noise predictor  $\tilde{\boldsymbol{\varepsilon}} = \boldsymbol{\varepsilon}_{\text{pos}} + w[\boldsymbol{\varepsilon}_{\text{pos}} - \boldsymbol{\varepsilon}_{\text{neg}}]$  with optimal weight  $w^*(\mathbf{x}, t)$ ,  $\boldsymbol{\varepsilon}_{\text{pos}}$  ( $w = 0$ ), and  $\boldsymbol{\varepsilon}_{\text{neg}}$  ( $w = -1$ ).



Figure 14: Generated samples from the human evaluation where RCT introduced artifacts.

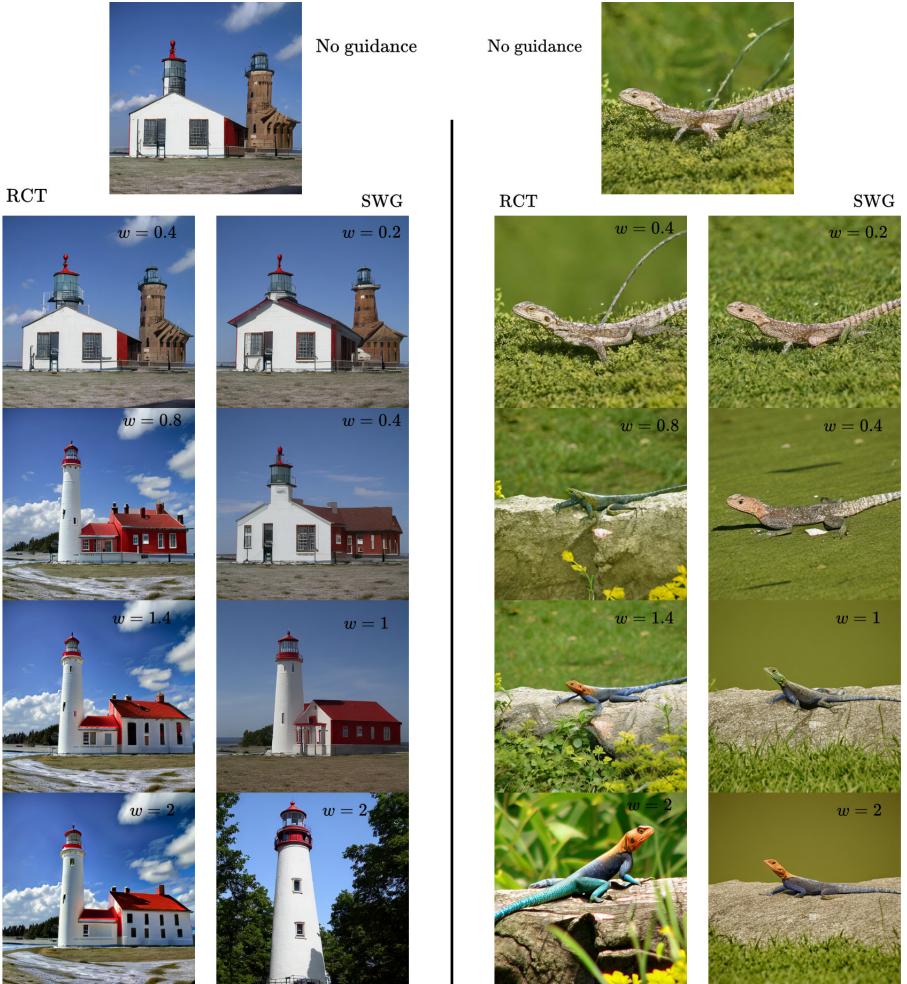


Figure 15: More examples with different guidance scales  $w$  for RCT (left) and SWG (right).

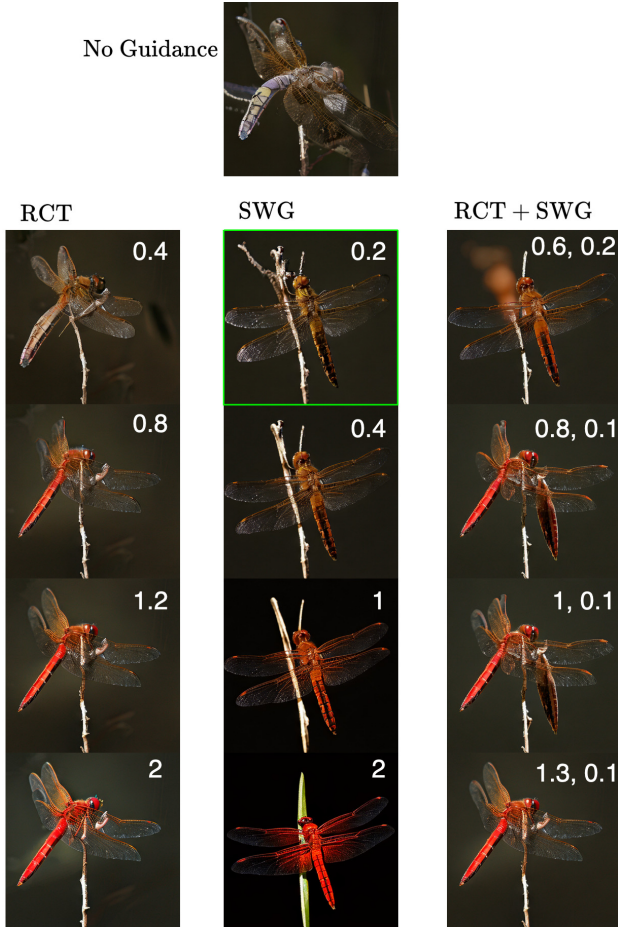


Figure 16: Generated EDM2-XXL  $512 \times 512$  samples using no guidance, RCT (left), SWG (center), and RCT+SWG (right). The guidance scales are shown in white on the top right corner of the image. The green box shows the sample that was used in the main paper, Figure 1.